

Document downloaded from:

<http://hdl.handle.net/10251/148908>

This paper must be cited as:

Malerød-Fjeld, H.; Clark, D.; Yuste Tirados, I.; Zanón González, R.; Catalán-Martínez, D.; Beeaff, D.; Hernández Morejudo, S.... (2017). Thermo-electrochemical production of compressed hydrogen from methane with near-zero energy loss. *Nature Energy*. 2(12):923-931. <https://doi.org/10.1038/s41560-017-0029-4>



The final publication is available at

<https://doi.org/10.1038/s41560-017-0029-4>

Copyright Nature Publishing Group

Additional Information

Thermo-electrochemical production of compressed hydrogen from methane with near-zero energy loss

Authors:

H. Malerød-Fjeld¹, D. Clark^{1,2}, I. Yuste-Tirados¹, R. Zanón³, D. Catalán-Martinez³, D. Beeaff¹, S. H. Morejudo¹, P. K. Vestre¹, T. Norby², R. Haugsrud², J. M. Serra^{3,*}, C. Kjøseth^{1,*}

¹CoorsTek Membrane Sciences AS, NO-0349 Oslo, Norway

²Department of Chemistry, Centre for Materials Science and Nanotechnology, University of Oslo, NO-0318 Oslo, Norway

³Instituto de Tecnología Química (ITQ), Universitat Politècnica de València (UPV) - Consejo Superior de Investigaciones Científicas (CSIC), 46022 Valencia, Spain.

*e-mail: jmserra@itq.upv.es; ckjolseth@coorstek.com

Conventional production of hydrogen requires large industrial plants to minimise energy losses and capital costs associated with steam reforming, water-gas shift, product separation, and compression. Here we present a protonic membrane reformer (PMR) which produces high purity hydrogen from steam methane reforming in a single-stage process with near-zero energy loss. We use a BaZrO₃-based proton-conducting electrolyte deposited as a dense film on a porous Ni composite electrode with dual function as a reforming catalyst. At 800 °C, we achieve full methane conversion by removing 99 % of the formed hydrogen, which is simultaneously compressed electrochemically up to 50 bar. A thermally-balanced operation regime is achieved by coupling several thermo-chemical processes. Modelling of a small scale (10 kg H₂ day⁻¹) hydrogen plant reveals an overall energy efficiency of >87 %. The results suggest that future declining electricity prices can make PMRs a competitive alternative for industrial-scale hydrogen plants integrating CO₂ capture.

Membranes that simultaneously enable chemical reaction and product separation hold promise for process intensification¹⁻³. Currently, the most energy efficient production pathway for hydrogen from methane combines steam reforming ($\text{CH}_4 + \text{H}_2\text{O} = 3\text{H}_2 + \text{CO}$, $\Delta H_{1073\text{K}} = 226 \text{ kJ mol}^{-1}$) and water-gas shift ($\text{CO} + \text{H}_2\text{O} = \text{H}_2 + \text{CO}_2$, $\Delta H_{1073\text{K}} = -34 \text{ kJ mol}^{-1}$) in a multistep process⁴, where heat management is crucial. The produced hydrogen is conventionally separated downstream using e.g. pressure swing absorption (PSA)⁵. Alternatively, hydrogen separation can be included in the steam reforming process using hydrogen selective membranes^{6,7} with the benefit of simultaneously separating hydrogen while shifting the thermodynamic equilibrium resulting in process intensification. Most practiced membranes are metallic, predominantly based on Pd or Pd-Ag alloys⁸. The separation is driven by the hydrogen partial pressure difference across the membrane, from which it follows that the pressure of the produced hydrogen is low, and further

compression requires multistage compressors, increasing both the capital as well as the energy costs.

Solid oxide electrochemical cells operating at high temperature can be used as fuel cells⁹, electrolyzers¹⁰, or membrane reactors for direct conversion of low- to higher-value chemicals¹. Potential application of high temperature proton conductors as the functional membrane in energy conversion technologies dates back almost forty years when proton conductivity in acceptor-doped BaCeO₃ was reported and its application to steam electrolysis was claimed¹¹. In the years to follow, publications classified several acceptor-doped alkaline earth cerates and zirconates as proton conductors with diverse potential uses in electrochemical cells, membrane reactors for dehydrogenation, or sensors¹²⁻¹⁵. However, the cerates are vulnerable towards decomposition in CO₂ levels even as low as for ambient air, jeopardizing long-term durability. In comparison, acceptor-doped barium zirconates exhibit superior chemical stability, but it was not until their high bulk proton conductivity was resolved^{16,17} that the true potential could be envisioned. The refractory nature of these ceramics made component fabrication remain challenging, but this has been overcome with the recent development of reactive sintering processes and partial substitution of some of the Zr with Ce¹⁸⁻²⁰, forming basis for the stability and functionality required for the different components in the protonic membrane reformer.

Herein, we report an electrochemically-driven protonic membrane reformer (PMR) (Fig. 1a) that realises four process steps simultaneously within a 400 μm length scale; it extracts hydrogen from the reforming side and shifts a thermodynamically-limited reaction sequence towards full conversion of methane, delivers heat to the strongly endothermic reaction through the electrical operation of the membrane—acting as separator and compressor—(Fig. 1b), compresses hydrogen directly at the sweep side of the membrane, and produces high-purity hydrogen. The combination of these functions in a single spatially-integrated stage confers high overall energy efficiency, process simplicity and compactness.

The protonic membrane reformer

The reformer is a tubular cell, 10 mm outer diameter, composed of a dense 30-μm-thick BaZr_{0.8-x-y}Ce_xY_yO_{3-δ} (BZCY) proton-conducting electrolyte sandwiched between two porous electrodes of BZCY and Ni (Fig. 2a and Methods). At 800 °C and a steam pressure of 1 bar, BZCY exhibits pure proton (H⁺) conductivity of 10 mS cm⁻¹ (Supplementary Fig. 1). By applying a voltage and hence current across the electrolyte, hydrogen is selectively extracted from the inner steam methane reforming chamber, reaching hydrogen production rates of 25 mL min⁻¹ cm⁻² at 4 A cm⁻² (Fig. 2b), operating essentially at the theoretical Faradaic limit and with an area specific resistance of 0.4 Ω cm² (Supplementary Fig. 1). The 800-μm-thick Ni-BZCY porous support provides catalytic activity towards reforming (Supplementary Fig. 2) comparable to Ni-based commercial catalysts. During the cell reduction, Ni nanoparticles—reaction sites—are exsolved from the oxide structure (Supplementary Fig. 2) and the activity towards steam reforming is potentially further enforced via surface-protonic water-activation mechanisms²¹.

Fig. 2c shows the evolution of methane conversion and yield to CO and CO₂ as a function of the imposed hydrogen recovery at 800 °C and 10 bar. Essentially full equilibrium shift of the steam

reforming and water-gas shift reactions (99.9 % methane conversion) is accomplished by selectively extracting hydrogen along the reactor length. Methane is completely converted to high-purity hydrogen and wet CO₂ (98 % selectivity towards CO₂) in two separate gas streams. The PMR is highly competitive with Pd-based membrane reformers on hydrogen production rate and recovery as well as methane conversion and, advantageously, the PMR delivers compressed hydrogen with an impurity level of <4 ppm at 50 bar (Supplementary Fig. 4).

The cell voltage (U_{cell}) and associated electrical power required during operation rely on reversible and irreversible terms²². The former is described by the Nernst voltage (U_{Nernst}) originating from the hydrogen partial pressure gradient across the proton conducting electrolyte and provides a direct estimate of the energy cost of the concomitant hydrogen separation and compression. The irreversible term is related to the overpotential of the resistance to proton migration through the ceramic electrolyte ($U_{\text{electrolyte}}$) and overpotentials related to the kinetics of splitting and re-combining hydrogen at the electrodes ($U_{\text{electrode}}$). When exposed to steam, the oxygen vacancies in the crystal lattice of the BZCY electrolyte annihilate by hydration and are replaced by protonic charge carriers residing as hydroxide ions¹⁶, $\text{H}_2\text{O} + \text{v}_\text{O}^\bullet + \text{O}_\text{O}^\times = 2\text{OH}_\text{O}^\bullet$. Under the PMR operating conditions, high steam pressure results in high concentration of protons and hence high and pure protonic conductivity, even at 800 °C, while ceramic proton conductors otherwise must operate below 600 °C under ambient humidity²³. The high-temperature operation exponentially enhances proton mobility, and additionally reduces proton trapping²⁴ and grain boundary resistance²⁵, resulting in high protonic conductivity and thus a low $U_{\text{electrolyte}}$.

The electrode composition and microstructure are tailored for high electronic and protonic conduction and gas transport. Moreover, the Ni electrocatalyst is highly active towards hydrogen redox reactions, altogether providing excellent electrode performance with a total area specific electrode polarization resistance lower than 0.1 Ω cm² during operation (Supplementary Fig. 1). Fig. 3a shows the cell voltage breakdown into these different terms, obtained under experimentally optimised conditions (see Methods). Only U_{Nernst} augments with increasing hydrogen delivery pressure, while $U_{\text{electrolyte}}$ decreases. The latter stems from the simultaneous rise in hydrogen delivery pressure and steam pressure (from 0.1 to 1.6 bar, corresponding to a mole fraction of H₂O of 4 %) that boosts the electrolyte proton conductivity. The electrode overpotential $U_{\text{electrode}}$ remains essentially constant at ~30 mV, indicating that the hydrogen desorption process is not affected by rising delivery pressures, even up to 40 bar. A long-term test (800 h) of the PMR showed stable operation in terms of catalytic activity, hydrogen production and ASR although coarsening of Ni particles is detected after 1800 h in operation (See Supplementary Fig. 1d and Fig. 2b-d).

Microscale integrated heat management

The reaction heat $\Delta_R H$ required to form hydrogen from methane and water scales linearly with the production rate. The heat evolved from the galvanic operation of the membrane distributes along the length of the membrane and originates from compression and Joule contributions, displaying, respectively, linear and quadratic dependencies with the production rate (Fig. 1b and 3b). Because the chemical reactions occur in the vicinity of the membrane, the endothermic and exothermic processes are spatially-coupled at microscale. Thermo-fluid dynamic (TFD) simulations reveal that methane conversion via steam reforming dominates in the first part of the reactor tube followed by water-gas shift (WGS), overall generating minor changes in temperature along the tube length (Fig. 4b). Furthermore, the minor radial concentration gradients demonstrate appropriate gas diffusion (Fig. 4c). The microscale thermal integration eliminates the need for complex heat management in the reaction zone, and the PMR can therefore be considered as a thermally autonomous unit.

TFD sensitivity studies evidence that the most important parameters governing the operation of the electrochemical reformer are the magnitude of the cell resistance R_{cell} and, to a less extent, the WGS reaction kinetics (Supplementary Fig. 5), while steam reforming kinetics and cell support porosity are less determining. Significantly lower or higher R_{cell} leads to strong temperature gradients along the cell and, as a consequence, the operation regime (methane flow and applied current) should be re-adjusted to reach again a thermally-balanced and autonomous operation (Supplementary Fig. 6).

System heat integration was evaluated by simulating the complete reformer plant (*cf.* Supplementary Fig. 7 and 8) as a function of hydrogen production rate by changing the applied current. Reactant pre-heating and steam generation are attained by heat-exchange with hydrogen and CO₂ outlet-streams, the total heat required by the system was found to be 38 % larger than for $\Delta_R H$ only (Fig. 3b, dotted line). The energy Sankey diagram (Fig. 3c) illustrates the impact of the thermal integration together with heat recovery on the system energy efficiency, as most of the energy entered is embedded in the compressed hydrogen product.

Increasing hydrogen delivery pressure amplifies the heat evolved from the membrane, linked to the U_{Nernst} enhancement (Fig. 3b, solid lines). Our analysis shows that, for the chosen set of parameters, heat balance is reached at 6.3, 4.0, and 2.9 kg day⁻¹ m⁻² for 3, 50, and 200 bars, respectively, operating at the highest efficiency of ~91 %. (Fig. 3b). Higher production rates diminish the efficiency as the galvanic operation heat exceeds the reforming heat demand. For a given system size, the production rate can be adjusted by the applied current, allowing for production flexibility yet at efficiencies higher than 70 %. For instance, the production rate at 200 bar can be tripled while remaining at an efficiency exceeding 75 %.

PMR process techno-economics

To assess the practical implications of the PMR technology, we have compared the operating energy costs of PMR with two established hydrogen production technologies; a water electrolyser (WEL) and a steam methane reforming (SMR) facility. Currently, SMR holds the

highest market share of the hydrogen generation technologies and the magnitude of the CO₂ emissions per kg of produced H₂ is lower than that exhibited by WEL using electricity supplied from grid (Supplementary Fig. 11). Hydrogen production from oil and coal are also important pathways today, but we have not included them in our analysis as we consider them substantially less competitive in terms of CO₂ emissions.

In Fig. 5a-c we have evaluated the effect of the electricity-to-natural gas price ratio and carbon tax on the operating energy cost for a centralised plant in different scenarios. SMR has the competitive advantage for low natural gas prices and WEL gains competitiveness with decreasing electricity prices. As a hybrid technology, PMR finds its cost-competitive domain between those of SMR and WEL. In a first scenario (Fig. 5a), the assumption is that electricity will come from the grid while the cost of CO₂ emissions is based on the electricity consumption reflecting the emissions from the current mix of power plants in Europe (Supplementary Figure 11 and Methods). In this scenario, the use of electricity will not lead to any reduction in CO₂ emissions compared to the use of natural gas, and the lower carbon footprint for PMR is directly related to the high energy efficiency. In the future, electricity may be produced from renewable sources with near-zero CO₂ emissions, and this scenario is depicted in Fig 5b, where WEL becomes more competitive when a carbon tax is imposed on PMR and SMR. Another potential pathway to low-carbon hydrogen production is carbon capture and storage (CCS). In Fig. 5c, a substantial amount of the CO₂ produced by PMR and SMR is captured and stored (while electricity in this scenario continues to be emission-free and hence no CO₂ emissions are assigned to WEL). To illustrate the techno-economic impact of different CCS strategies to SMR, two sub-domains are introduced. SMR-1 represents a low-cost CCS option where CO₂ is only captured from the product stream, while SMR-2 is a higher-cost approach that also captures CO₂ from the process flue gas stream, resulting in higher CO₂ capture efficiency (66 and 90 % respectively, Supplementary Fig. 11). SMR with partial CO₂ capture (SMR-1) is the most favourable technology at low CO₂ taxation, SMR with full capture (SMR-2) is more competitive at higher carbon tax, and PMR continues to hold a competitive advantage over the other technologies for intermediate electricity-to-natural gas price ratios.

The quantitative analysis of the operating energy costs (Fig. 5d) for the different technologies uses energy prices for Norway as an example of a country with low-cost renewable electricity and natural gas (cf. Supplementary Fig. 11). Such an energy scenario, we believe, is likely to represent the future energy situation with increasing amounts of cheap renewable electricity in combination with abundant natural gas. The analysis reveals that PMR and SMR are the less sensitive technologies to energy prices, with operating energy cost of WEL, SMR and PMR calculated to 2.2, 0.9, and 0.9 \$ kg⁻¹, respectively.

In addition to the operating energy costs, the capital expenses of the plant and the maintenance costs contribute to the overall production cost. An experimentally realised segmented PMR reactor with sealed interconnects and gas manifolds (Supplementary Fig. 12) was taken as the fundamental building block for calculating the cost of a PMR plant (conceptual design shown in Supplementary Fig. 13). The benchmark SMR-1 plant was equipped with an amine scrubber on the hydrogen rich product stream, thereby removing 66 % of the produced CO₂, while the PMR plant was assumed to remove all CO₂ since the outlet gas is so rich in CO₂, and therefore suitable for compression to 153 bar without further purification. The analysis of the estimated cost for

centralised hydrogen production plants (Fig. 5e and Supplementary Table 2) reveals that WEL has substantially higher plant costs than SMR-1 and PMR, while the baseline cost of SMR-1 was calculated to about 20 % less than of PMR.

Employing the baseline plant cost, Norwegian energy prices, carbon capture employed and CO₂ taxed at 50 \$/tonne, the breakdown to the overall hydrogen production cost was estimated (Fig. 5f) and it emphasizes that operating energy costs dominate for all technologies. The hydrogen production cost of WEL, SMR-1 and PMR is calculated to 2.4, 1.2, and 1.1 \$ kg⁻¹, respectively, showing that PMR is price competitive, even at large scale and lower CO₂ taxes.

A general advantage of electrochemical technologies is scalability towards lower production volumes without substantial loss of efficiency. A compact PMR hydrogen generator with capacity of 25 kg day⁻¹ can be designed (Supplementary Fig. 14), e.g. suitable for fuelling of fuel cell electric vehicles (FCEVs). At this scale, our modelling suggests the PMR generator will make FCEVs a competitive alternative to battery electric vehicles (BEVs) on a well-to-wheel basis when electricity and natural gas are sourced from grids (Fig. 6a-b for distributed H₂ generation), while representing a reduction in CO₂ emissions compared to internal combustion engines (ICEs, 65 % reduction), and BEVs (21% reduction).

A bottom-up manufacturing cost analysis of the hydrogen generator (Supplementary Fig. 14) estimates the total cost of the generator, including mark-up, to 23.7 k\$. The PMR can operate at different production rates, with higher efficiencies at lower production rates (Fig. 3b), and when operated at 7.7 and 25 kg day⁻¹, the efficiency is 88 and 67 %, respectively, referred to as lean and max operation. The equipment cost (including maintenance) for lean and max operation is 2.9 and 0.9 \$ kg⁻¹ (Fig. 6c) at 40 % utilization (cf. Supplementary Fig. 14), while the energy cost is 2.2 \$ kg⁻¹ (lean) and 3.7 \$ kg⁻¹ (max), in sum causing the max operation to be the most cost-effective option at 40 % utilization. However, at 90 % utilization, the difference in equipment cost between lean and max is less prominent so that the hydrogen cost at lean operation is 0.5 \$ kg⁻¹ less than at max operation. Variations in both natural gas and electricity price (Fig. 6d) strongly affect PMR hydrogen production costs (\pm 50 %) regardless of the operation mode.

Challenges that will need to be overcome before commercial use of PMR technology is realised include reaching complete thermal integration and autonomous operation for compact generators and engineering miniaturized generator designs to maximize compactness and minimise manufacturing costs. To investigate the potential of an improved reactor design beyond the baseline design reported here, the membrane packing density (membrane area/reactor volume) was increased by allowing shorter tube-to-tube distances and smaller tube diameters (Supplementary Fig. 15). This higher packing density reduces the need for expensive steel for the pressure vessels, reaching a hydrogen production cost < 3.2 \$ kg⁻¹, even at 40 % utilization. It may also be noted, that the main raw materials used for the manufacturing of the PMR technology (Supplementary Figure 13) mostly comprise common bulk materials. To install a 1 000-tonne day⁻¹ PMR facility, it is estimated that the consumption of raw materials (sulphates and oxides of Ba, Zr, Ce and Y) that are used in the membrane will be less than 1 % of the present annual global production (Supplementary Fig. 15).

Conclusions

We have demonstrated a steam methane reformer based on a high temperature proton ceramic electrolyte with Ni composite electrodes, producing separate streams of CO₂ and electrochemically-compressed hydrogen. The thermal coupling at micro-scale of endothermic chemical reactions and electrical overpotential losses facilitates a spatially-uniform thermally-balanced operation regime, yielding enhanced process operational simplicity and energy conversion efficiency over other systems.

The protonic membrane reformer (PMR) technology allows significant process intensification for compressed hydrogen production. High energy efficiency together with the hybrid nature of the PMR technology, using approximately 1/3 electricity and 2/3 natural gas, enables us to decrease the carbon footprint compared to traditional SMR, especially when using electricity from renewable sources. For industrial-scale hydrogen production at geographic locations with access to infrastructure for CO₂ storage or use, the PMR technology benefits also from producing a nearly-pure stream of CO₂ as by-product, enabling effective carbon capture, use and storage (CCUS) as a pathway to achieve carbon neutrality.

As the PMR technology is scalable it could be deployed in a distributed manner, requiring only natural gas or biogas, water and electricity. Assuming that the price of natural gas remains below the price of petroleum and electricity, our modelling suggests that the PMR technology could make FCEVs running on hydrogen the lowest cost automotive powertrain.

Methods

Fabrication of ceramic membranes. Tubular membrane electrode assemblies were prepared by co-sintering of a coated, extruded substrate. The extrudate consisted of a mixture of ceramic powders and an aqueous binder system. All powders, except nickel oxide, were first milled to a nominal particle size of approximately 0.3 μm . The nickel oxide was used as-received with a particle size of 1 μm . The ceramic component of the extrudate was a blend of 60 wt. % NiO (*NiO-F*, Fuel Cell Materials) and 40 wt. % of a mixture of BaSO_4 (*Blanc Fixe N*, Solvay), CeO_2 (*CE-OX-O3*, American Elements), ZrO_2 (AMR) and Y_2O_3 (HJD International), the latter in molar ratios to yield $\text{BaZr}_{0.7}\text{Ce}_{0.2}\text{Y}_{0.1}\text{O}_{3-\delta}$ (BZCY72) on decomposition and reaction. After drying, the green substrate was coated with a slurry consisting of the perovskite precursors, binders, and an organic solvent. The stoichiometry of the precursors was adjusted to produce either $\text{BaZr}_{0.7}\text{Ce}_{0.1}\text{Y}_{0.2}\text{O}_{3-\delta}$ (BZCY71) or $\text{BaZr}_{0.8}\text{Ce}_{0.1}\text{Y}_{0.1}\text{O}_{3-\delta}$ (BZCY81) on decomposition. For BZCY71 electrolytes, the powders were identical to those used for the substrate as described above. For BZCY81 electrolytes, all starting powders were obtained from Alfa Aesar and were ball milled for three days to a nominal average particle size of 5 μm . Coating was achieved by spray coating multiple layers while rotating the substrate using an automated spray coater (*Max-800*, Ultrasonic Systems, Inc). Finally, an outer electrode was applied by dip coating the two-layered green tube in a slurry containing mixture of 40 to 50 % ceramic powders and an aqueous binder system. The composition of the slurry was otherwise identical to that used to fabricate the substrate. The three-layered green ceramic tubes were then hang-fired in a muffle furnace using tubular kiln furniture as support to a temperature of 1600 to 1650 $^{\circ}\text{C}$ for 5 to 10 hours. The subsequent reduction was done at 1000 $^{\circ}\text{C}$ for 24 h in a flow of 5 % H_2 balanced with Ar yielding an open porosity of 26 vol.% estimated using Archimedes method. The resulting Ni particles were in the range 20–30 μm . Individual segments with electrode lengths of 0.5, 2, 4 and 10 cm, the exact length being determined by the experimental variable being investigated, were sealed to a riser using a glass ceramic seal designed to match the thermal expansion coefficient of the membrane electrode assembly to ensure that the samples were positioned in a uniform hot zone during experiments. The other end of the tube was capped using a similar glass ceramic material. Finally, a Ni ink (Ni-I, FuelCellMaterials) was hand brushed onto the surface of the outer electrode and fired at 950 $^{\circ}\text{C}$, serving as current collector.

Reactor setup. The tubular reactor setup consisted of the inner membrane tube and an outer steel reactor tube (EN 1.4959, I.D. = 15.8 mm). The tubes were assembled onto a 316 SS Swagelok-based system providing electrical contacts and feedthroughs for thermocouples and gases. Thermocouples (TCs) were placed inside the tube and outside the outer reactor tube at the top, middle and bottom of the segments. By utilizing these TCs, the heating zones of the reactor furnace were adjusted to an axial temperature difference of less than 10 $^{\circ}\text{C}$. A Ni tube (O.D = 4.6 mm) served as the gas feed and current collector for the reforming side. To ensure contact between the membrane and Ni tube, Ni wool (American Elements) was inserted into the end of the tube. For outer current collection, Cu wire (diameter = 0.25 mm) was wrapped around the electrode as current-carrying wires from the electrode and to a connection point outside the furnace.

PMR experiments. The experiments were conducted in a setup provided by AP Miniplant where gas and liquid flows supplied to both reactor sides were controlled by thermal mass flow controllers. Steam was generated using an electrically heated evaporator. To avoid steam

condensation, all gas lines, valves and the reactor furnace were inside a heating cabinet operated at 165 °C. The feed gas consisted of a mixture of 23.4 % CH₄, 60.6 % H₂O, 14.7 % H₂ and 1.2 % He, resembling a gas composition from a pre-reformer (except CO and CO₂) operating at 495 °C and 10 bar with an initial steam-to-carbon ratio (S/C) of 2.5. He was used as internal standard. The inlet sweep gas was a mixture of 80 % Ar and 20 % H₂O, also maintained at 10 bar.

A micro gas chromatograph (Model 490, Varian) measured the concentrations of He, H₂, CH₄, CO and CO₂ of the gas line outlets of the reforming and hydrogen side. Conversion of CH₄ into CO and CO₂ was calculated by closing the carbon balance. Coke formation was not observed in any of the experiments and has therefore not been considered. Hydrogen recovery, *HR*, was calculated based on the measured hydrogen flows F_{H_2} of both outlets as

$$HR = \frac{F_{H_2}^{II}}{F_{H_2}^I + F_{H_2}^{II}} \quad (1)$$

where I and II denote the outlets of the reforming and hydrogen side.

DC current-voltage measurements and impedance spectroscopy were conducted using a Gamry Reference 3000 with a Reference 30K Booster allowing currents up to 30 A. The voltage was monitored continuously under galvanostatic operation. Impedance spectra were recorded in the frequency range 10 kHz to 0.01 Hz with oscillation voltage between 50–200 mV both under open-circuit conditions and under 0.5 A cm⁻². The spectra were fitted using the software EqC²⁶. Because the setup only allowed for one separate electrical connection to each electrode, the electrical data was corrected for parasitic contributions by measuring the resistance of the current carrying wires under the same conditions in a separate experiment.

For the experiment reported in Fig. 3a, a feed gas mixture of 60 % H₂ (500 mL min⁻¹) and 40 % H₂O (268 mg min⁻¹) was used at a total pressure of 5 bar, while the sweep gas inlet was fed with 500 mL min⁻¹ H₂ and 15 mg min⁻¹ H₂O (3.6 % H₂O) and the total pressure was increased step-wise. The high flow rates assured that the change in the Nernst voltage (U_{Nernst}) with and without hydrogen extraction currents (0.5 A cm⁻²) was less than 3 %. To determine the different voltage losses that contribute to the overall cell voltage U_{cell} , the DC voltage was measured under open circuit voltage and load (0.5 A cm⁻²) and taken as U_{Nernst} and U_{cell} . The electrolyte contribution $U_{electrolyte}$ was extracted from impedance spectra recorded under load (see details below), and the electrode contribution U_{el} was calculated using the relation $U_{cell} = U_{Nernst} + U_{electrolyte} + U_{electrode}$.

A long-term durability study was conducted using a stoichiometric titration cell setup²⁷ with a feed gas consisting of humidified ($p_{H_2O} \sim 0.03$ bar) 50 mL min⁻¹ H₂, 25 mL min⁻¹ Ar, and a sweep gas consisting of humidified ($p_{H_2O} \sim 0.03$ bar) 100 mL min⁻¹ 5% H₂ (bal. Ar). The 1.59 cm² cell was operated at 800 °C at 0.5 A cm⁻² with the H₂ flux measured to be constant (~ 3.3 mL min⁻¹ cm⁻²; Faradaic efficiency ~ 0.97) over the 2000 hour operation. A second long-term stability study (Supplementary Fig. 2b) was performed under standard PMR operating conditions for 750+ hours using a cell with an area of ≈ 33 cm² under a 10 A load.

Microscopy. Scanning electron microscopy (SEM) was conducted on a tube cross-section which had been mounted in epoxy (Allied EpoxySet) and polished to finish of 0.06 μm (colloidal silica). Backscatter electron (BSE) micrographs were taken with an FEI Quanta 200 FEG-ESEM at 15 keV in low-vacuum mode (60 Pa) to reduce sample charging. Scanning transmission electron

microscope (STEM) micrographs were taken with a JEOL 2100F 200 keV field emission S/TEM equipped with a Gatan Orius 200D CCD camera and Oxford X-Max-80 SDD energy dispersive x-ray (EDS) detector (0.23 srad collection angle). S/TEM compositional EDS maps were collected with a dwell time of 100 μ s of BaL α , CeL α , ZrK α , YK α , OK α , and NiK α and were analyzed using Oxford Instruments Aztec 2.1 (SP1) software.

Thermo-fluid dynamic simulations. All equations used are given in Supplementary Table 1.

The TFD model was built using the kinetics proposed elsewhere^{28 29} for methane steam reforming reaction and water gas shift reaction. The process considers an adiabatic setup using the reactions heats, the heat from the joule effect and the heat from the hydrogen compression. Secondary current distribution was used to model the electrochemistry considering 100% for the faradic efficiency. Averaged-mixture model was used to characterize gas diffusion phenomena in the reformer chamber. Navier-Stokes equations using the respective correction for the porous domain were used to model the gas flows. The rest of the CFD modelling methodology is explained in the Supplementary Methods.

Thermodynamic modelling. Global thermodynamic model calculations in the protonic membrane reformer were carried out in a commercial chemical process engineering software platform³⁰. The hydrogen extraction membrane was simulated using a sequential model, dividing the reactor axially into $-n$ multi-sub-reactors and $-n-1$ sub-separator. A first Gibbs reactor is followed by a series of selective hydrogen separators with constant extraction in each, and a Gibbs reactor to re-equilibrate all the reaction products upon hydrogen extraction. An excess of catalyst was assumed to guarantee that equilibrium is reached and that kinetic factors play a subordinate role in limiting the reactions.

Species considered in the simulation were CH₄, C₂H₆, C₃H₈, H₂, O₂, CO, CO₂ and H₂O. The simulations were run at constant temperature and pressure. The molar flows of all the components at the outlet were used to compute CH₄ conversion, yields towards the different products and hydrogen recovery. Key results of the thermodynamic study are summarized in Supplementary Fig. 7.

PMR system modelling. To assess the energy balance, we considered the heat supplied and required by the PMR operating at 800 °C, 10 bar, S/C = 2.5 and a HR of 98 %. This condition results in high conversion (99.998 %) and high CO₂ yield (89.3 %, Supplementary Fig. 7), while still maintaining a reasonable mole fraction of hydrogen in the tail gas (0.049). The average hydrogen partial pressure on the reforming side along the length of the membrane, $p_{H_2}^I$, was calculated to 3.29 bar.

Heat, henceforth given on an area specific basis, is supplied by the heat evolving from the membrane, originating from contributions relating to the separation of hydrogen from one reactor side to the other

$$U_{\text{sep}}I = R_{\text{cell}}I^2 \quad (5)$$

and compression of hydrogen

$$U_{\text{Nernst}}I = \frac{RT}{2F} \ln \left(\frac{p_{H_2}^{II}}{p_{H_2}^I} \right) I \quad (6)$$

R_{cell} denotes the area specific resistance, I the current, and F is Faradays constant.

The inlet of the PMR is a mixture of methane and steam at 450 °C (from pre-reformer) and then heated up to 800 °C. The outlet of the pre-reformer will contain 12 % hydrogen, which ensure sufficient hydrogen extraction from the beginning of the tube (Supplementary Fig. 7). The heat exchange between the pre-reformer and reformer is performed with an excess of heat (~22 %) given by the membrane.

The PMR model was adjusted by varying the current density to work in lean operation, where the heat evolved and heat required are as equal as possible (Supplementary Fig. 8). Both a distributed and centralised hydrogen production system were modelled in Supplementary Fig. 9 and 10, respectively. The process includes the PMR model described above, a steam generation unit, a heat exchanger system, and a mechanical compression stage to deliver hydrogen at high pressure (the latter is omitted in centralised case and in Figure 3b and Supplementary Fig. 8, where only electrochemical compression is considered).

System efficiency (Fig. 3b) was calculated as

$$Efficiency (\%) = \frac{F_{H_2} \times HHV_{H_2}}{F_{NG} \times HHV_{NG} + W_{electric}} \cdot 100 \quad (7)$$

Where F_n is the flow rate of component n , HHV_n is higher heating value of component n , and W is the electric power consumption. For the energy efficiency calculations, losses associated to transformation and rectification of the input alternating current is not included.

Techno-economic evaluation. The operating energy costs of the PMR technology were compared with two other established technologies, a water electrolyser (WEL) and a conventional steam methane reformer (SMR). The effect of the price ratio of electricity and natural gas was investigated as a variable. Electricity was either provided from the grid or from renewables without CO₂ emissions. The “EU28-mix” was assumed for grid electricity, which has a CO₂ emission intensity of 76.6 g CO₂-eq per MJ of produced electricity³¹. An EU mix was also assumed for natural gas, and losses associated to production, transportation and conditioning (13 g CO₂-eq per MJ of natural gas) were included to the combustion, resulting in a total emission intensity of 69 g CO₂-eq/MJ³². Carbon tax was normalized to the emission intensity of natural gas. That is, spending 1 MJ of grid electricity was taxed $76.6/69 = 1.11$ times higher to that of spending 1 MJ of natural gas. The carbon tax was set as a fraction of the price of natural gas, from 0 to 1.

Hydrogen production was considered either from a large centralised facility (typically more than 100 tonne H₂ per day) or from a small-scale distributed facility (typically 10 kg day⁻¹). Naturally, the electrolyser only uses electricity, while the centralised SMR was assumed to use 2 and 0.6 % electricity with and without carbon capture, respectively³³. For distributed SMR, it was assumed that 8 % of the total energy needed was supplied from electricity when delivering hydrogen at 5 bar³⁴. With compression to 200 bar, the percentage increases to 13 %.

Carbon capture was considered a feasible option for the centralised facilities. For PMR, the tail gas content of CO₂ is 96.4 % (Supplementary Fig. 10) after steam is condensed out to less than 0.05 %, which is likely to confer with quality criteria for CO₂ transportation in pipelines³⁵. Energy losses are then mainly related to the compression of CO₂ (only 2.0 % loss in the total efficiency).

For SMR, CO₂ from the hydrogen rich stream after WGS reactors was removed before the pressure swing adsorption (PSA) with amine scrubbing, while CO₂ removal from the flue gas exiting the furnace of the reformer was not considered due to lower CO₂ content, and it was therefore assumed that 66 % of the total amount of CO₂ could be captured³³. A loss of 3 % of the overall efficiency when imposing capture was calculated. It was assumed that hydrogen was compressed to 26 bar, while CO₂—if captured—was pressurized to 153 bar to ensure transport as a supercritical fluid. The energy costs of compression were included in the calculations.

For system efficiencies, we assumed 68 % for WEL³⁶ (26 bar), 76 % for centralised SMR (26 bar), 70 % for distributed SMR (5 bar). Losses when hydrogen was compressed were calculated in ASPEN and included when relevant. A schematic representation of the evaluation process and the assumed numbers to assess the operating energy costs are shown in Supplementary Fig. 11.

The manufacturing cost of distributed and centralised PMR was calculated bottom-up, based on a segmented multi-tube PMR reactor as the fundamental ceramic stack component (Supplementary Fig. 12). The stacks, together with the enclosing pressure vessel, are termed a single engineering unit (SEU). The conceptual design for the centralised and distributed production facilities, including the characteristics of the SEUs, are given in Supplementary Fig. 13 and 14, respectively.

The manufacturing cost comprised of raw and indirect materials cost, labour cost and tooling cost. The baseline of the cost model was taken from an existing pilot plant; however, it was assumed that the SEUs were manufactured in a highly automated plant with continuous production and low scrap rates. Labour costs were assumed to be \$ 50 000 per year, and 50 % overhead was added to this. The tooling cost includes the depreciation of the equipment involved in the manufacturing, and it was assumed the equipment was fully depreciated over the units manufactured in the plant. Assumptions for the prices of the most important raw materials and the rolled throughput yield for the manufacturing of the components are given in Supplementary Fig. 13 and 14.

The complete cost of the centralised SMR and PMR plants were based on previously obtained data³³ and adjusted for inflation from the date of the report (12 % from 2010), and the cost breakdown is given in Supplementary Tables 2. Engineering, construction management, and contingency were then added, and the total is termed the plant cost. Pre-production costs, cost of land and financing costs were not included. For PMR, a DC power supply cost of 80 \$/kW was assumed. Lower and higher cost ranges were calculated by adjusting contingencies, and for PMR also the membrane module cost, as summarized in Supplementary Table 2.

The cost of the WEL plant was calculated based on a system electrolyser cost (in \$/kW), taken from the literature³⁶, assuming future reductions in the system cost (Supplementary Table 2). In addition, cost elements comprising compression and grid connection were added, and low and high range were calculated by adjusting the electrolyser system cost (Supplementary Table 2d). Finally, the contribution of the plant to the total hydrogen production cost was calculated by taking into account the life time of the plant and the availability, and fixed operation and maintenance costs (Supplementary Table 2).

A well-to-wheel analysis for a fuel cell electric vehicle (FCEV-PMR) running on hydrogen produced from distributed PMR was carried out to calculate the energy and CO₂ emission per distance travelled. The analysis considered well-to-plug, plug-to-tank, and tank-to-wheel contributions, and a schematic of the methodology and the numbers used is shown in Supplementary Fig. 11. The outcome of the analysis was compared with an internal combustion engine (ICE) vehicle running on gasoline with direct injection spark ignition technology, vehicle FCEV with hydrogen produced from a water electrolyser (FCEV-WEL) and a battery electric vehicle (BEV), for which well-to-wheel data were directly extracted from previous works^{37 38}

Data availability. The data that support the plots within this paper and other findings of this study are available from the corresponding author upon reasonable request

References

- 1 Morejudo, S. H. *et al.* Direct conversion of methane to aromatics in a catalytic co-ionic membrane reactor. *Science* **353**, 563-566, doi:10.1126/science.aag0274 (2016).
- 2 Chu, S. & Majumdar, A. Opportunities and challenges for a sustainable energy future. *Nature* **488**, 294-303 (2012).
- 3 Logan, B. E. & Elimelech, M. Membrane-based processes for sustainable power generation using water. *Nature* **488**, 313-319 (2012).
- 4 Rostrup-Nielsen, J. R. Catalysis and large-scale conversion of natural gas. *Catalysis Today* **21**, 257-267, doi:[http://dx.doi.org/10.1016/0920-5861\(94\)80147-9](http://dx.doi.org/10.1016/0920-5861(94)80147-9) (1994).
- 5 Voss, C. Applications of Pressure Swing Adsorption Technology. *Adsorption* **11**, 527-529, doi:10.1007/s10450-005-5979-3 (2005).
- 6 Gallucci, F., Fernandez, E., Corengia, P. & van Sint Annaland, M. Recent advances on membranes and membrane reactors for hydrogen production. *Chemical Engineering Science* **92**, 40-66, doi:<http://dx.doi.org/10.1016/j.ces.2013.01.008> (2013).
- 7 Boeltken, T., Wunsch, A., Gietzelt, T., Pfeifer, P. & Dittmeyer, R. Ultra-compact microstructured methane steam reformer with integrated Palladium membrane for on-site production of pure hydrogen: Experimental demonstration. *Int. J. Hydrog. Energy* **39**, 18058-18068, doi:<http://dx.doi.org/10.1016/j.ijhydene.2014.06.091> (2014).
- 8 Al-Mufachi, N. A., Rees, N. V. & Steinberger-Wilkens, R. Hydrogen selective membranes: A review of palladium-based dense metal membranes. *Renewable and Sustainable Energy Reviews* **47**, 540-551, doi:<http://dx.doi.org/10.1016/j.rser.2015.03.026> (2015).
- 9 Sengodan, S. *et al.* Layered oxygen-deficient double perovskite as an efficient and stable anode for direct hydrocarbon solid oxide fuel cells. *Nature Materials* **14**, 205-209, doi:10.1038/nmat4166 (2015).
- 10 Myung, J.-h., Neagu, D., Miller, D. N. & Irvine, J. T. S. Switching on electrocatalytic activity in solid oxide cells. *Nature* **537**, 528-531, doi:10.1038/nature19090 (2016).
- 11 Iwahara, H., Uchida, H., Ono, K. & Ogaki, K. Proton conduction in sintered oxides based on BaCeO₃. *Journal of the Electrochemical Society* **135**, 529-533, doi:10.1149/1.2095649 (1988).
- 12 Hamakawa, S., Hibino, T. & Iwahara, H. Electrochemical methane coupling using proton conductors. *J. Electrochem. Soc.* **140**, 459-462 (1993).
- 13 Bonanos, N., Knight, K. S. & Ellis, B. Perovskite solid electrolytes: Structure, transport properties and fuel cell applications. *Solid State Ionics* **79**, 161-170, doi:10.1016/0167-2738(95)00056-c (1995).
- 14 Norby, T. Solid-state protonic conductors: principles, properties, progress and prospects. *Solid State Ionics* **125**, 1-11, doi:10.1016/s0167-2738(99)00152-6 (1999).

- 15 Kreuer, K. D. On the development of proton conducting materials for technological applications *Solid State Ionics* **97**, 1-15 (1997).
- 16 Kreuer, K. D. Aspects of the formation and mobility of protonic charge carriers and the stability of perovskite-type oxides. *Solid State Ionics* **125**, 285-302, doi:10.1016/s0167-2738(99)00188-5 (1999).
- 17 Kreuer, K. D. Proton-conducting oxides. *Annual Review of Materials Research* **33**, 333-359, doi:10.1146/annurev.matsci.33.022802.091825 (2003).
- 18 Tao, S. W. & Irvine, J. T. S. A stable, easily sintered proton-conducting oxide electrolyte for moderate-temperature fuel cells and electrolyzers. *Advanced Materials* **18**, 1581+, doi:10.1002/adma.200502098 (2006).
- 19 Wang, H., Peng, R., Wu, X., Hu, J. & Xia, C. Sintering Behavior and Conductivity Study of Yttrium-Doped BaCeO₃-BaZrO₃ Solid Solutions Using ZnO Additives. *Journal of the American Ceramic Society* **92**, 2623-2629, doi:10.1111/j.1551-2916.2009.03204.x (2009).
- 20 Coors, W. G. Co-Ionic Conduction in Protonic Ceramics of the Solid Solution, BaCe_(x)Zr_(y-x)Y_(1-y)O_{3-δ}. Part I: Fabrication and microstructure. *Advances in Ceramics - Synthesis and Characterization, Processing and Specific Applications*, DOI: 10.5772/30672, doi:DOI: 10.5772/30672 (2011).
- 21 Manabe, R. *et al.* Surface Protonics Promotes Catalysis. *Scientific Reports* **6**, 38007, doi:10.1038/srep38007 (2016).
- 22 Rohland, B., Eberle, K., Ströbel, R., Scholta, J. & Garcke, J. Electrochemical hydrogen compressor. *Electrochimica Acta* **43**, 3841-3846, doi:[http://dx.doi.org/10.1016/S0013-4686\(98\)00144-3](http://dx.doi.org/10.1016/S0013-4686(98)00144-3) (1998).
- 23 Kochetova, N., Animitsa, I., Medvedev, D., Demin, A. & Tsiakaras, P. Recent activity in the development of proton-conducting oxides for high-temperature applications. *Rsc Advances* **6**, 73222-73268, doi:10.1039/c6ra13347a (2016).
- 24 Yamazaki, Y. *et al.* Proton trapping in yttrium-doped barium zirconate. *Nature Materials* **12**, 647-651, doi:10.1038/nmat3638 (2013).
- 25 Kjølseth, C. *et al.* Space-charge theory applied to the grain boundary impedance of proton conducting BaZr_{0.9}Y_{0.1}O_{3-δ} (delta). *Solid State Ionics* **181**, 268-275, doi:10.1016/j.ssi.2010.01.014 (2010).
- 26 Boukamp, B. A. . *Equivalent circuit for Windows Ver. 1.0* (2003).
- 27 Grover Coors, W. A stoichiometric titration method for measuring galvanic hydrogen flux in ceramic hydrogen separation membranes. *J. Membr. Sci.* **458**, 245-253, doi:<http://dx.doi.org/10.1016/j.memsci.2014.01.071> (2014).
- 28 Zeppieri, M., Villa, P. L., Verdone, N., Scarsella, M. & De Filippis, P. Kinetic of methane steam reforming reaction over nickel- and rhodium-based catalysts. *Applied Catalysis A: General* **387**, 147-154, doi:<http://dx.doi.org/10.1016/j.apcata.2010.08.017> (2010).
- 29 Wang, B., Zhu, J. & Lin, Z. A theoretical framework for multiphysics modeling of methane fueled solid oxide fuel cell and analysis of low steam methane reforming kinetics. *Applied Energy* **176**, 1-11, doi:<http://dx.doi.org/10.1016/j.apenergy.2016.05.049> (2016).
- 30 Skutil, K. & Taniewski, M. Some technological aspects of methane aromatization (direct and via oxidative coupling). *Fuel Processing Technology* **87**, 511-521, doi:<http://dx.doi.org/10.1016/j.fuproc.2005.12.001> (2006).
- 31 Overview of electricity production and use in Europe. *European Environment Agency*, doi:http://www.eea.europa.eu/ds_resolveuid/76139b352a5e4663905a78ca388cd8da (2016).
- 32 Edwards, R., Larive, J.-F., Rikeard, D. & Weindorf, W. Well-To-Wheels analysis of future automotive fuels and powertrains in the european context, Well-to-Tank Report Version 4.a, JEC Well-to-Wheels Analysis. *JRC Technical Reports* doi:10.2790/95629 (2014).

- 33 Cho, V. H., Hamilton, B. A. & Kuehn, N. J. Assessment of Hydrogen Production with CO₂ Capture Volume 1: Baseline State-of-the-Art Plants. *National Energy Technology Laboratory DOE/NETL-2010/1434*, doi:http://www.canadiancleanpowercoalition.com/pdf/SMR9%20-%20H2_Prod_Vol1_2010.pdf (2010).
- 34 Schjøberg, I. *et al.* IEA-HIA Task 23 Small-scale Reformers for On-site Hydrogen Supply. *International Energy Agency-Hydrogen Implementing Agreement*, doi:http://ieahia.org/pdfs/Task23_Final-Report_ISBN.aspx (2012).
- 35 de Visser, E. *et al.* Dynamis CO₂ quality recommendations. *International Journal of Greenhouse Gas Control* **2**, 478-484, doi:<http://dx.doi.org/10.1016/j.ijggc.2008.04.006> (2008).
- 36 Bertucciolo, L. *et al.* Study on development of water electrolysis in teh EU, Development of Water Electrolysis in the European Union. *FCH JU Publication*, doi:http://www.fch.europa.eu/sites/default/files/study%20electrolyser_0-Logos_0_0.pdf (2014).
- 37 Edwards, R. *et al.* Well-To-Wheels analysis of future automotive fuels and powertrains in the european context, Well-to-Wheels Report Version 4.a, JEC Well-to-Wheels Analysis. *JRC Technical Reports* doi:10.2790/95533 (2014).
- 38 Huss, A., Maas, H. & Hass, H. Well-to-Wheels analysis of future automotive fuels and powertrains in teh european context, Tank-to-Wheels Report Version 4.0, JEC Technical Reports. *JRC Technical Reports*, doi:10.2788/40409 (2013).

Acknowledgments

This work was supported by the Research Council of Norway (grant 256264) and Spanish Government (SEV-2016-0683 grant). NORTEM is acknowledged for access to transmission electron microscopes.

Authors contributions

H.M.F., D.C, R.Z., and C.K. performed the experiments. H.M.F., J.M.S., R.H., D.C. P.K.V., T.N., and C.K. designed the experiments. D.B fabricated the tubular membrane electrode assembly. H.M.F., C.K., R.H., T.N. and J.M.S. analyzed electrochemical data. H.M.F., J.M.S., S.H.M., R.Z., and C.K. analyzed the catalytic data. I.Y.T. and D.C.M. designed and performed modelling studies. D.C. collected scanning and transmission electron microscope data. P.K.V. and C.K. initiated the project. H.M.F., D.C, I.Y.T, D.C.M., D.B., S.H.M., P.K.V., T.N., R.H., J.M.S. and C.K. wrote the manuscript, while all authors discussed the results and commented on the manuscript.

Additional information

Supplementary information is available

Reprints and permissions information is available at www.nature.com/reprints.

Correspondence and requests for materials should be addressed to J.M.S. (jmserra@itq.upv.es) or C.K. (ckjolseth@coorstek.com)

Competing interests

The authors declare no competing financial interests. Note that they do receive various forms of funding, employment and remuneration from CoorsTek Membrane Sciences.

Figure Legends and Tables

Figure 1 | Schematic of the protonic membrane reformer. a, Methane (CH_4) is reformed with steam (H_2O) on the reaction side. H_2 is separated by protonic transport from the reaction side (with lower partial pressure of hydrogen— $p_{\text{H}_2}^{\text{I}}$) to the hydrogen side ($p_{\text{H}_2}^{\text{II}} > p_{\text{H}_2}^{\text{I}}$) and directly compressed as a result of the applied voltage. Red, white, and grey atoms represent H, O, and C, respectively. **b,** Energy balance and system micro-integration for operation at 800 °C for a feed inlet of one mole CH_4 . Heat for the endothermic reaction is supplied from separation and compression

Figure 2 | Protonic membrane reformer for production of compressed hydrogen. a, Schematics of the protonic membrane reactor. Methane is steam reformed (SMR) to CO and H_2 over Ni particles inside the ceramic tube. Hydrogen is transported as protons to outer side, while CO is converted to CO_2 by water-gas shift (WGS) reaction. Outlet composition is mainly CO_2 and steam. The hydrogen produced is of high purity and compressed *in-situ*. The net endothermic chemical reaction is balanced with the heat evolved from the galvanic operation of the electrochemical cell. Red, white, and grey atoms represent H, O, and C, respectively. Top SEM micrograph insets correspond to the cathode/electrolyte/anode structure (left), composite reforming anode (center) and composite cathode (right), including chemical and electrochemical reactions, depicted schematically. **b,** Hydrogen production rate versus current density at 800 °C, 10 bar, $S/C=2.5$. Steam pressure on hydrogen side inlet was 2.0 bar. Red line indicates Faradaic limit. Additional data is given in Supplementary Fig. 3. **c,** Conversion, yield of CO_2 and CO versus hydrogen recovery at 800 °C, 10 bar, $S/C = 2.5$. Steam pressure on hydrogen side inlet was 0-2.0 bar. Data points from six experiments. Solid lines obtained from thermodynamic modelling calculated from theory (Supplementary Figure 7). Additional data are given in Supplementary Figure 3.

Figure 3 | Break down of voltage losses and microthermal integration at 800 °C. a, Cell (U_{cell}), electrolyte (U_{BZCY}), electrode ($U_{\text{electrode}}$) and Nernst voltage (U_{Nernst}) versus hydrogen delivery pressure. Reaction conditions: $p_{\text{H}_2} = 3$ bar, and $p_{\text{H}_2\text{O}} = 2$ bar on reaction side; current density of 0.5 A cm^{-2} . Steam concentration on hydrogen side kept constant at 4 %. At 42 bar, area specific resistance is 0.69 W cm^2 . Solid line is the calculated Nernst voltage. **b,** Top: Heat evolved from membrane at indicated pressures and heat required by protonic membrane reformer (PMR, dashed line) and SMR and WGS reactions (dotted line) versus hydrogen production rate at a hydrogen recovery (HR) of 98 %. $R_{\text{cell}} = 0.5 \text{ W cm}^2$. Bottom: Overall system efficiency versus hydrogen production rate at 3, 50 and 200 bar as modelled by ASPEN simulations. $HR = 98$ %. Current density (bottom x-axis) and hydrogen production rate (top x-axis) are directly proportional. **c,** Sankey energy diagram for a 10 kg day^{-1} hydrogen production

facility based on system modelling (see Methods), closing the energy input (Electricity and Natural Gas) and output (thermal losses, utility losses and hydrogen) in the overall energy balance. The heat recovery and microthermal integration are the specific properties of PMR resulting in the overall high energy efficiency.

Figure 4 | Thermo-fluid dynamic simulations. a, Schematics of the protonic membrane reactor. Black arrows indicate the direction of gas flow in the inner chamber of the reactor and white arrows indicate the direction of hydrogen flow. **b**, Radial-symmetric volume distribution of temperature and zoom view of the electrode length at a current density of 0.4 A cm^{-2} , $T_{\text{inlet}} = 735 \text{ }^\circ\text{C}$, inner chamber pressure: 10 bar; outer pressure chamber: 40 bar, $F(\text{H}_2/\text{H}_2\text{O}/\text{CH}_4) = 12.5/51.7/20 \text{ mL min}^{-1}$. **c**, Distribution of methane molar fraction (inner reforming chamber) at a current density of 0.4 A cm^{-2} , $T_{\text{inlet}} = 735 \text{ }^\circ\text{C}$, inner chamber pressure: 10 bar; outer pressure chamber: 40 bar, $F(\text{H}_2/\text{H}_2\text{O}/\text{CH}_4) = 12.5/51.7/20 \text{ mL min}^{-1}$.

Figure 5 | Techno-economic evaluation of centralised hydrogen production plant. a-c, Domains indicate economically preferred technology based on operating energy costs for water electrolysis (WEL), PMR and steam methane reformer (SMR). Primary variable is the price ratio of electricity to natural gas, and secondary variable is a carbon tax, set as a fraction of the price of natural gas. Comparisons of plant with electricity from (a) grid, (b) electricity from renewable energy (RE), and (c) electricity from RE and with carbon capture (CC). See Methods for details. **d**, Sensitivity analysis of natural gas (NG) and electricity price on the operating energy cost of WEL, SMR and PMR. Baseline prices were set to $0.18 \text{ } \$ \text{ Nm}^{-3}$ and $0.035 \text{ } \$ \text{ kWh}^{-1}$ for NG and electricity, and the price ranges spanned from 0.08 to $0.7 \text{ } \$ \text{ Nm}^{-3}$ and 0.02 to $0.15 \text{ } \$ \text{ kWh}^{-1}$. Baselines indicated with circles. **e**, Plant cost for WEL, SMR-1 and PMR. SMR-1 and PMR plants with carbon capture facilities. Baseline indicated with dotted line. Ranges are calculated using different assumptions for capital costs. See Methods and Supplementary Table 2 for additional details on baseline and ranges. **f**, Hydrogen production cost for WEL, SMR-1 and PMR with carbon capture facilities, using $0.18 \text{ } \$ \text{ Nm}^{-3}$ and $0.035 \text{ } \$ \text{ kWh}^{-1}$ as price for NG and electricity.

Figure 6 | Techno-economic evaluation of distributed hydrogen production. a-b, Well-to-wheel analysis of (a) energy and (b) greenhouse gas emissions for an internal combustion engine (ICE), a battery electric vehicle (BEV) and a fuel cell electric vehicle (FCEV) running on hydrogen from a water electrolyser (WEL) and PMR. Energy is divided into tank-to-wheel and well-to-tank. See Methods for details. **c**, Hydrogen production cost for PMR operating in three different modes. NG price: $0.28 \text{ } \$ \text{ Nm}^{-3}$. Electricity price: $0.10 \text{ } \$ \text{ kWh}^{-1}$. Mode 1: Baseline hydrogen generator, and lean operating mode (high system efficiency of 88 %). Mode 2: Baseline hydrogen generator and maximum operating mode (highest hydrogen flux while maintaining 67 % system efficiency). Mode 3: Advanced hydrogen generator with higher packing density and lean operating mode. Utilization refers to the time percentage over a year that the PMR is operating. See Methods for additional details. **d**, Sensitivity analysis of natural gas (NG) and electricity price on hydrogen production cost for PMR operated in mode 1, 2 and 3. Baseline prices were set to $0.28 \text{ } \$ \text{ Nm}^{-3}$ and $0.10 \text{ } \$ \text{ kWh}^{-1}$ for NG and electricity, and the price ranges spanned from 0.2 to $0.7 \text{ } \$ \text{ Nm}^{-3}$ and 0.05 to $0.15 \text{ } \$ \text{ kWh}^{-1}$. Utilization was set to 90 %.

Thermo-electrochemical production of compressed hydrogen from methane with near-zero energy loss

H. Malerød-Fjeld¹, D. Clark^{1,2}, I. Yuste-Tirados¹, R. Zanón³, D. Catalán-Martinez³, D. Beeaff¹, S. H. Morejudo¹, P. K. Vestre¹, T. Norby², R. Haugsrud², J. M. Serra^{3,*} and C. Kjøseth^{1,*}

¹CoorsTek Membrane Sciences AS, NO-0349 Oslo, Norway.

²Department of Chemistry, Centre for Materials Science and Nanotechnology, University of Oslo, NO-0318 Oslo, Norway.

³Instituto de Tecnología Química (ITQ), Universitat Politècnica de València (UPV) - Consejo Superior de Investigaciones Científicas (CSIC), 46022 Valencia, Spain.

*e-mail: jmserra@itq.upv.es; ckjolseth@coorstek.com

This supplement contains:

Supplementary Methods

Supplementary Figure 1 – 15

Supplementary Tables 1 – 2

Supplementary References

Supplementary Methods

Fixed bed reactor experiments. 0.5 g of catalyst (ground and sieved tube support) were diluted with 5 g of SiC and loaded to the reactor. An additional SiC bed (7 g) was placed on top of the catalyst fixed bed. The catalyst was pre-treated in situ in a flow of N_2 (50 mL min^{-1}) from room temperature up to $700 \text{ }^\circ\text{C}$ ($7 \text{ }^\circ\text{C min}^{-1}$). Then, the catalyst was pre-reduced using a gas mixture of $H_2:N_2$ (1:1 vol. ratio), and the temperature was increased up to $900 \text{ }^\circ\text{C}$ ($7 \text{ }^\circ\text{C min}^{-1}$) and kept for 12 h. After the activation, the temperature was reduced to $800 \text{ }^\circ\text{C}$ ($7 \text{ }^\circ\text{C min}^{-1}$) and a gas mixture of $CH_4:N_2:H_2$ (4.75:0.25:5 vol. ratio) was introduced. In addition, this gas mixture was humidified by saturation in a heated bubbler at $93 \text{ }^\circ\text{C}$ (corresponding to $p_{H_2O} = 0.78 \text{ bar}$). Upon temperature stabilisation, H_2 is not further fed and the resulting feed mixture is humidified $CH_4:N_2$ (9.5:0.5 vol. ratio) at a flow of 25 mL min^{-1} . N_2 was used as analytic internal standard. The experiments were carried out at 1.1 bar. The unconverted methane and the formed products (H_2 , CO , CO_2) were analyzed online using a gas chromatograph (Bruker 450-GC) equipped with five packed columns (Molsieve 5A, Hayesep Q, Molsieve 13X, Hayesep Q and Hayesep N), one capillary column (WCOT BR-1) and three detectors (2 TCD and FID). Methane conversion, products selectivity and yield were calculated on carbon basis. Equal amount of a state-of-the-art catalyst, Haldor-Topsøe R-67-7H, was evaluated in the same experimental setup using the same procedure.

Thermo-fluid dynamic simulations. All equations used are given in Supplementary Table 1.

Fluid flow model

On the reforming side, we consider laminar flow in both the open volume and in the Ni-cermet. The equation governing the fluid flow in the open volume is the Navier-Stokes equation (M1-M2, and M3-M4 in the porous cermet region). Regarding the fluid density, a mixture of ideal gases was considered for the internal gas and pure hydrogen for the external open volume. For the dynamic viscosity, the Wilke model¹ (equation M6) was used for the internal gas and pure H_2 for the external chamber. The source term (Q_{br} in M3) of the mass balance in the internal chamber was calculated considering the hydrogen extraction (from the current, applying Faraday's law). The porosity and permeability are two key factors that govern the fluid flow in the porous region and the permeability for a packed bed with randomly distributed spherical particles was calculated using the Carman-Kozeny model and the stated particle size and porosity mode² (equation M13). Feed gases were composed of a mixture of methane (24 %), hydrogen (15 %) and steam (61 %) supplied at different total inlet flow rates. For the external chamber and in the external electrode boundary, the hydrogen exchange was defined considering the faraday law.

Transport of species in the internal chamber

Considering the gas velocity in the reactor, the species are moving in a convective process where, in the porous support body, the reactions and the hydrogen extraction take place. The transport of the species was modelled using the mixture-averaged diffusion model (M8-M12, M14).

Kinetics

The kinetic model includes the reactions of steam methane reforming and the water-gas shift reaction (r_{SMR} and r_{WGS} , respectively) (equations M29-M32). The kinetics of the SMR reaction (M32) have been modelled using the works of Zeppieri et al.³ and Wang⁴. An equilibrium-limited rate expression was used to model the kinetics of the WGS reaction³⁻⁵, considering first order to carbon monoxide and steam (to model possible local limitations inside the internal catalyst bed). Equilibrium constants of reactions r_{MSR} and r_{WGS} , respectively, were calculated from thermodynamic

data obtained from ASPEN PLUS v8.8 (M30 and M31).

Electrochemistry

The hydrogen is electrochemically pumped from the internal chamber to the external chamber by the imposed electric current. The electrochemistry was governed by the secondary current distribution model (M15 – M18). A faradaic efficiency of 100 % was assumed.

For the anode and cathode, the half-cell reactions are:



The voltage balance equation relates the cell voltage to all overpotential losses that occur during operation (M19). The reversible voltage for both electrode reactions (r_{anode} and r_{cathode}) was calculated using the Nernst equation (M20).

Different values have been tested for the global resistance of the electrical device considering the experimental results as reference. Finally, R_{cell} was evaluated as a function of temperature, using $0.5 \Omega \text{ cm}^2$ at $800 \text{ }^\circ\text{C}$ as the starting point and an activation energy of $-50.4 \text{ kJ mol}^{-1}$ (M21).

Heat transfer

Heat generated (or required) for the different processes were calculated assuming perfect insulation. The model which governs the heat transfer is different depending on the medium (solid, fluid and porous) (M22-M24). Thermal energy was transferred by conduction and convection, while the radiation heat transfer was neglected due to its low impact. Furthermore, thermal properties of the membrane electrode assembly, hydrogen and the outer reactor tube (EN 1.4959) were used. Finally, alumina was considered for the tube riser. For the reforming side, the heat capacity and the thermal conductivity were calculated using the properties of pure gases (M25), using Wilke's approach (M26). In the adiabatic regime, several inlet-gas temperatures were considered.

Considering the adiabatic configuration of the process, the inlet gas temperature has been taken to achieve microthermal integration of the process and to reach the temperature around the membrane electrolyte assembly to be as isothermal as possible (and around $800 \text{ }^\circ\text{C}$).

Regarding the different heats generated (or consumed) in the process, the following phenomena were included: chemical reactions (r_{SMR} and r_{WGS}), Joule effect and the compression heat of H_2 across the solid electrolyte. As more current is imposed, the hydrogen extraction shifts the r_{SMR} and r_{WGS} towards increased conversion—more heat is required for the r_{SMR} reaction and produced from the r_{WGS} (M27). For the electrochemical process, the heat from the Joule effect was calculated considering the total resistance of the assembly and the current (M28).

Ordinary industrial gas compression takes place in a quasi-isentropic process. This type of compression causes high increases in temperature due to the change in the internal energy during the compression. In electrocompression, the hydrogen compression takes place across the electrolyte. Considering the thickness of the electrolyte ($30 \mu\text{m}$) the interaction of the electrochemical compression with the Joule effect and the heats of the internal reactions, the compression in the electrolyte should take place at quasi-isothermal conditions considering the thickness of the electrolyte. However, to simplify the process, isothermal compression assumption has been accepted to model the compression across the electrolyte.

Isothermal compression releases heat to avoid changes in the internal energy as indicated by the

first law of thermodynamics:

$$\text{Heat} = \Delta U - W_{\text{reversible}} \xrightarrow{\Delta U=0} \text{Heat} = -W_{\text{reversible}} \quad (3)$$

$$\text{Heat} = \int_{p_{H_2}^I}^{p_{H_2}^{II}} V dp = \int_{p_{H_2}^I}^{p_{H_2}^{II}} \frac{RT}{p} dp = RT \ln \left(\frac{p_{H_2}^{II}}{p_{H_2}^I} \right) \quad (4)$$

$$\text{Heat}_{\text{compression}} = RT \ln \left(\frac{p^{II}}{x_{H_2}(z, r) p^I} \right) \quad (5)$$

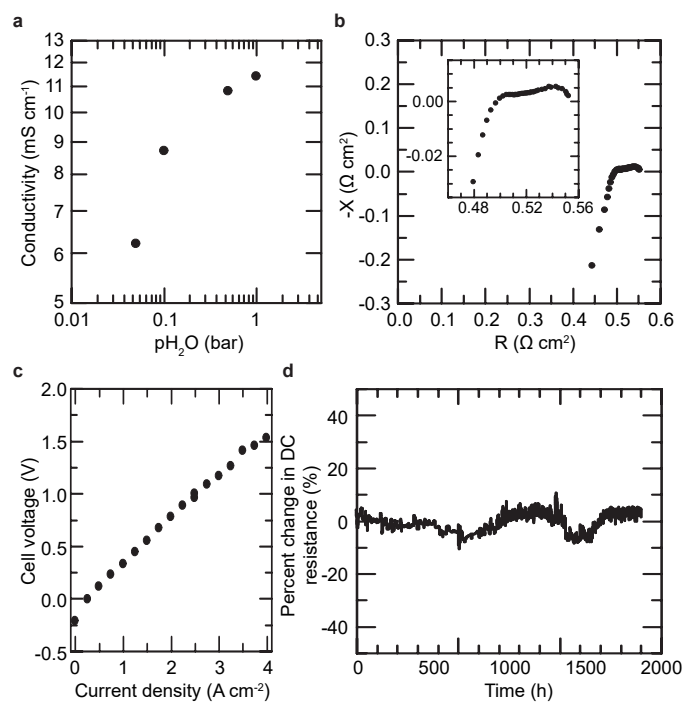
where U is the internal energy, W is the work, p^i is the pressure ($i = I$ internal chamber; $i = II$ external chamber), R is the constant of the ideal gases, x_{H_2} is the molar fraction of hydrogen in the internal chamber and (z, r) are the coordinates in the geometry.

Finally, the compression heat was calculated taking into account hydrogen state equations (M29). The isothermal compression was verified by calculating the internal and external surface temperatures showing approximately equal values.

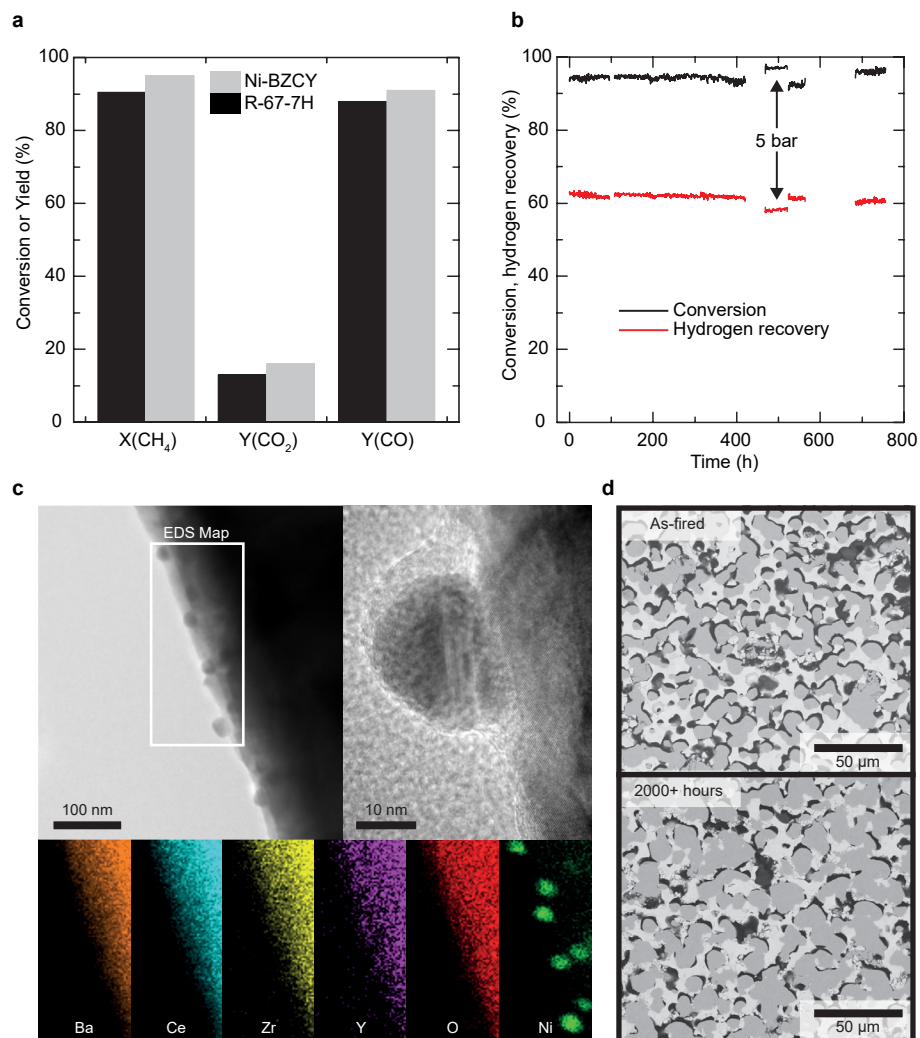
Some corrections were used to avoid local indeterminations. In the equations M20, M29, M30, M31 the molar fractions which appear in the denominator of the equations were corrected by adding 10^{-5} to avoid local problems in gas domains of the geometry.

Meshing and solver methodology

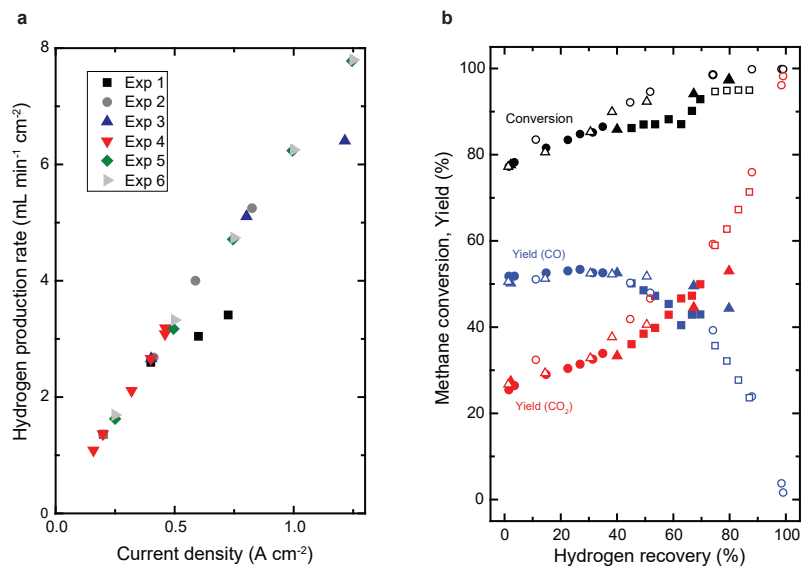
The problem can be greatly reduced from a computational point of view, as the axial symmetry geometry permits the use of 2D computational domains. Several interconnected domains were considered to represent the PMR geometry (Supplementary Fig. 5a). Supplementary Fig. 5b shows the meshing performed for the different domains. Adaptive mesh refinement was used to optimize the mesh, and the mesh use tetragonal division of the different domains. The calculations were carried out using the Parallel Direct Solver (PARDISO) with parameter continuation to assure convergence. The relative tolerance of the method is 0.001. A consistent stabilization criterion was chosen for all phenomena using streamline diffusion and crosswind diffusion. To improve the convergence of the system, the process was solved under isothermal conditions (at 800 °C) and then the solution was used as initial values for the complete process.



Supplementary Figure 1 | Properties of the electrochemical cell at 800 °C. **a**, Conductivity of the electrolyte in reducing atmosphere as a function of steam partial pressure. Electrolyte thickness was measured to be 25 μ m using scanning electron microscopy. **b**, Nyquist plot of in frequency range 8000 Hz to 0.04 Hz at bias of 0.6 A cm⁻², 10 bar and S/C = 2.5. Area specific resistance = 0.56 Ω cm². **c**, Current-voltage curve during PMR operation, 10 bar and S/C = 2.5. Area specific resistance from slope of curve is 0.42 Ω cm². **d**, Long-term durability under reducing conditions showing the change in DC cell resistance under constant applied current (0.5 A cm⁻²).



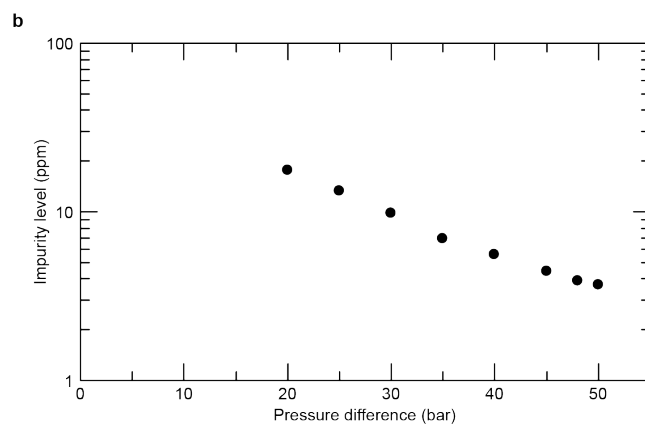
Supplementary Figure 2 | Characterisation of Ni-cermet catalyst. **a**, Conversion (X) and yields (Y) of the Ni-BZCY cermet (black) compared with state-of-the-art catalyst, Haldor-Topsøe R-67-7H, (grey) at 800 °C and 45600 mL g_{cat}⁻¹ h⁻¹. **b**, Long-term durability of membrane reactor under PMR conditions showing stable conversion and hydrogen recovery over a time period of 775+ hours. 800 °C, S/C = 2.5. Pressure was 10 bar, except from 440 h to 495 h, when pressure was 5 bar. **c**, S/TEM analysis of exsolved nanoparticles in the reduced Ni-BZCY cell support with energy dispersive x-ray spectroscopy (EDS) maps of the outlined white area in the top left micrograph and the bottom corresponding maps of Ba, Ce, Zr, Y, O and Ni. High-resolution S/TEM micrograph of ~20 nm Ni nanoparticle in the top right. **d**, SEM micrograph of polished cross-section of the Ni-BZCY cell support as-fired and after 2000+ hours of operation (sample from Supplementary Figure 1d).



Supplementary Figure 3 | Protonic membrane reformer for production of compressed hydrogen. a, Hydrogen production rate versus current density at 800 °C, 10 bar, S/C = 2.5. Data obtained from six different experiments. **b**, Conversion, yield of CO₂ and CO versus hydrogen recovery at 800 °C, 10 bar, S/C = 2.5. Data points from six different experiments are indicated with different symbols.

a

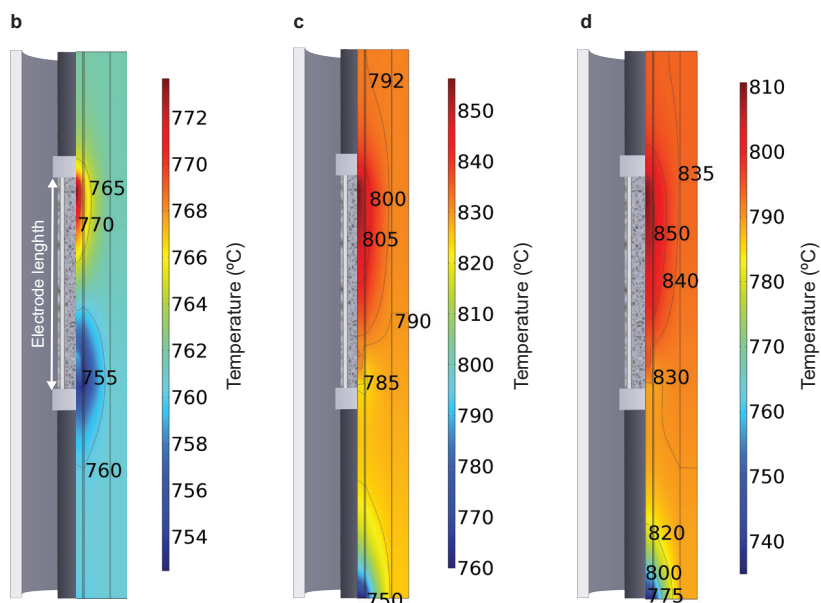
Reference	Temperature (°C)	j_{H_2} (mL min ⁻¹ cm ⁻²)	X_{CH_4} (%)	S_{CO_2} (%)	HR (%)
Tokyo Gas ^{6,7}	495–550	4–9	≤95	-	~95
Boeltken et al. ⁸	550	19	87	95	92
This study	800	25	99.9	98	99



Supplementary Figure 4 | PMR performance metrics. a, Comparison of hydrogen production rate (j_{H_2}), methane conversion (X_{H_2}), CO_2 selectivity (S_{CO_2}), and hydrogen recovery (HR) of PMR with Pd-based membrane reformers. **b,** Total concentrations of impurities in produced hydrogen versus pressure difference of hydrogen across membrane.

a

a_{ASR}	Current (A)	$T_{average}$ (°C)	$T_{distribution}$ (°C)	X_{CH_4}	S_{CO}	S_{CO_2}	HR (%)
0.5	12.0	761.7	760 ± 15	88.5	0.4	99.7	99.9
1	12.0	796.0	794 ± 19	90.5	0.9	99.1	99.7
2	12.0	842.9	839 ± 23	90.7	3.4	96.6	99.1



e

Porosity	$T_{average}$ (°C)	$T_{distribution}$ (°C)	X_{CH_4}	S_{CO}	S_{CO_2}	HR (%)
0.25	796.0	794 ± 19	89.6	0.9	99.1	99.7
0.50	796.0	793 ± 21	89.6	1.0	99.1	99.7
0.75	796.2	793 ± 24	89.7	1.1	98.9	99.7

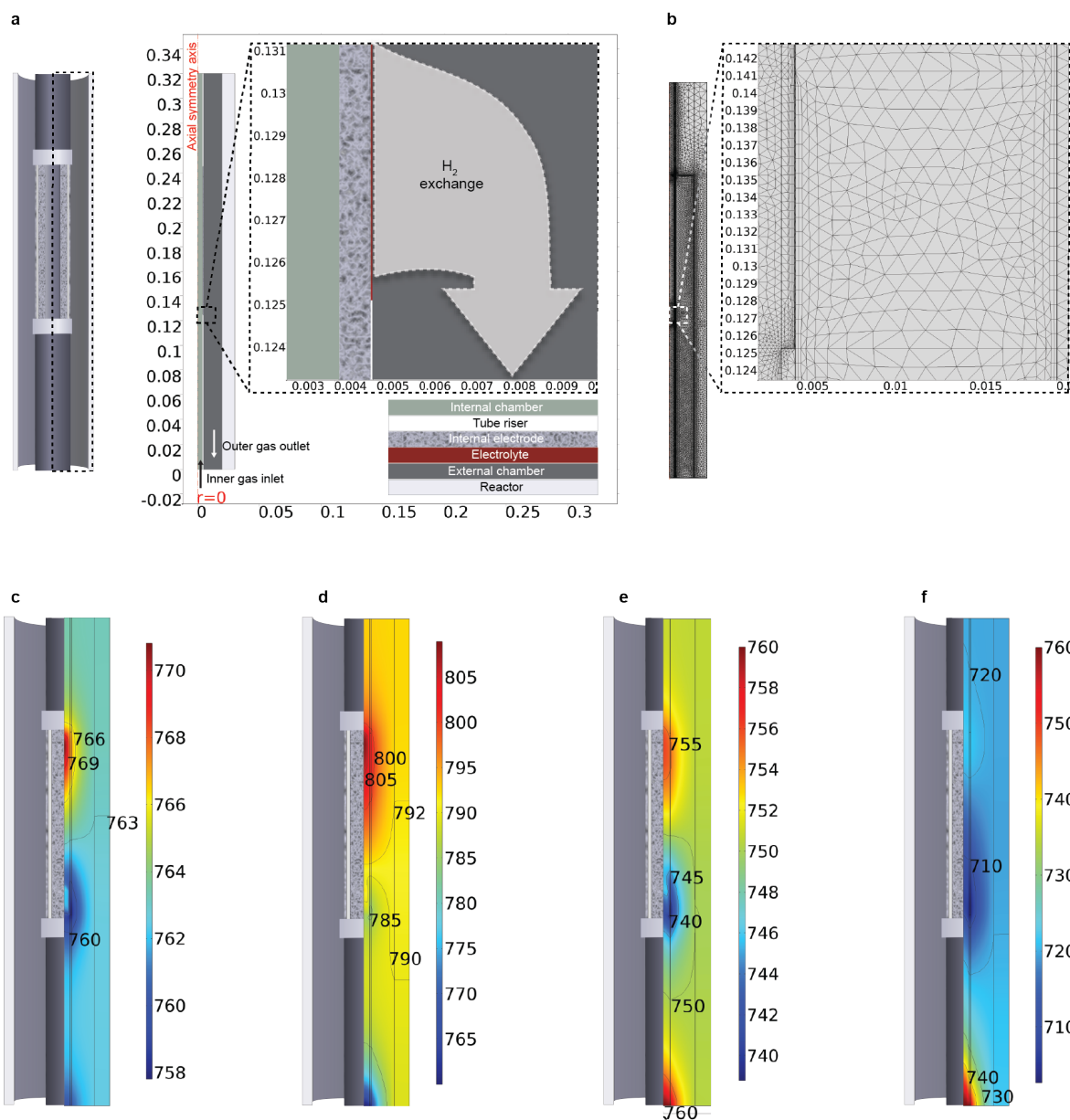
f

k_{SMR}	Current (A)	$T_{average}$ (°C)	$T_{distribution}$ (°C)	X_{CH_4}	S_{CO}	S_{CO_2}	HR (%)
x5	12.1	796.1	794 ± 19	90.6	1.1	98.9	99.7
x1	12.1	796.0	794 ± 19	90.5	0.9	99.1	99.7
x0.2	12.1	795.9	794 ± 19	90.2	0.3	99.7	99.9
x0.05	12.0	794.9	793 ± 18	89.8	0.2	99.8	99.9

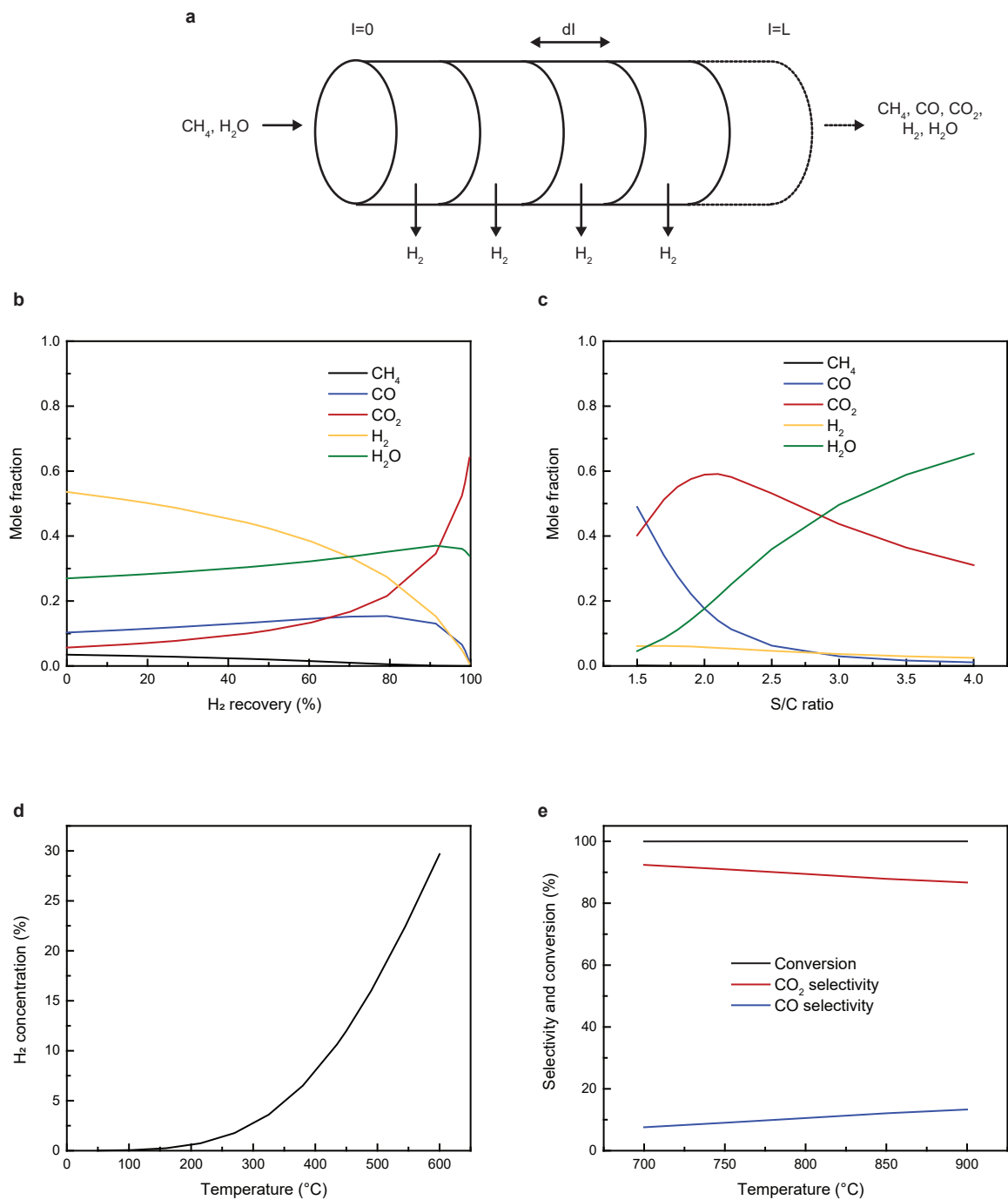
g

k_{WGS}	Current (A)	$T_{average}$ (°C)	$T_{distribution}$ (°C)	X_{CH_4}	S_{CO}	S_{CO_2}	HR (%)
x1	12.1	796.0	794 ± 19	90.5	0.9	99.1	99.7
x0.1	12.1	794.3	792 ± 24	90.5	0.8	99.2	99.8
x0.05	11.7	786.9	784 ± 23	90.3	6.9	93.1	97.7

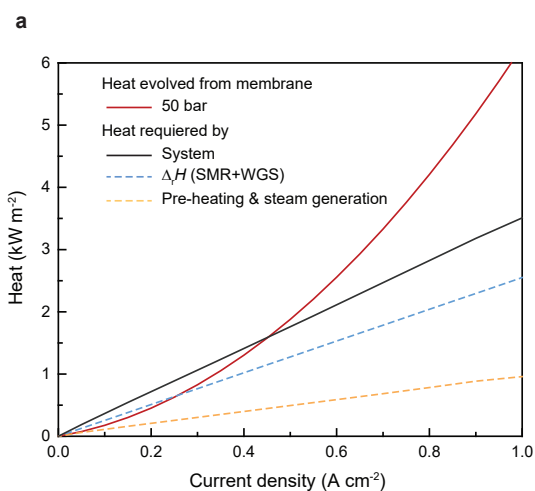
Supplementary Figure 5 | Thermo-fluid dynamic simulations : sensitivity study of the CFD model. a–d, Main results of the ASR variations, $ASR(T) = a_{ASR} \cdot ASR(T)$, at $T_{inlet} = 760$ °C, inner chamber pressure: 10 bar, outer pressure chamber: 10 bar, $F(H_2/H_2O/CH_4) = 12.5/51.7/20$ mL min⁻¹. Radial-symmetric volume distribution of temperature for $a_{ASR} = 0.5$ (b); $a_{ASR} = 1.0$ (c) $a_{ASR} = 2.0$ (d). **e**, Main results of the study of the inner electrode porosity at 0.4 A cm⁻², $T_{inlet} = 760$ °C, inner chamber pressure: 10 bar; outer pressure chamber: 10 bar, $F(H_2/H_2O/CH_4) = 12.5/51.7/20$ mL min⁻¹. **f**, Main results of the study of the methane steam reforming kinetics variations at $T_{inlet} = 760$ °C, inner chamber pressure: 10 bar; outer pressure chamber: 10 bar, $F(H_2/H_2O/CH_4) = 12.5/51.7/20$ mL min⁻¹. **g**, Main results of the study of the water gas shift kinetics variations at $T_{inlet} = 760$ °C, inner chamber pressure: 10 bar; outer pressure chamber: 10 bar, $F(H_2/H_2O/CH_4) = 12.5/51.7/20$ mL min⁻¹.



Supplementary Figure 6 | Thermo-fluid dynamic simulations. **a**, Schematics of the protonic membrane reactor and 2-D axial symmetry geometry adaptation of the PMR reactor. **b**, Mesh of the 2-D geometry. **c-f**, Radial-symmetric volume distribution of temperature for the study of different inner inlet flows at $T_{inlet} = 760$ °C, inner chamber pressure: 10 bar; outer pressure chamber: 10 bar, $F(H_2/H_2O/CH_4) = 6.25/20.8/10$ mL min⁻¹ and 0.2 A cm⁻² (**c**), $F(H_2/H_2O/CH_4) = 12.5/51.7/20$ mL min⁻¹ and 0.4 A cm⁻² (**d**), $(H_2/H_2O/CH_4) = 25/103.4/40$ mL min⁻¹ and 0.4 A cm⁻² (**e**), $F(H_2/H_2O/CH_4) = 50/206.8/80$ mL min⁻¹ and 0.4 A cm⁻² (**f**).



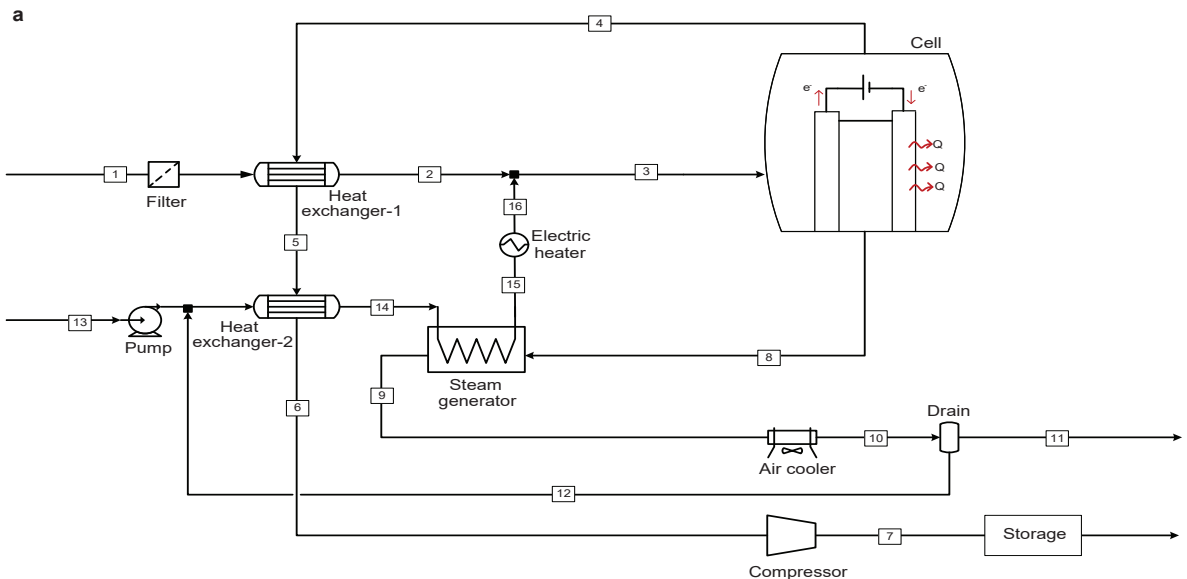
Supplementary Figure 7 | Thermodynamic model data. **a**, Schematic of the sequential model. **b**, Mole fraction of species from reforming outlet side with varying hydrogen recoveries at 800 °C, 10 bar and S/C = 2.5. **c**, Mole fraction of species from reforming outlet side with varying steam-to-carbon (S/C) ratios at 800 °C, 10 bar and HR = 98 %. **d**, Hydrogen concentration of the pre-reformer outlet with varying temperature at 10 bar and S/C = 2.5. **e**, Conversion, CO yield and CO₂ yield with varying temperature at 10 bar, S/C = 2.5 and HR = 98 %.



b

Model assumptions and parameters	
Hydrogen production	10 kg day ⁻¹
Hydrogen recovery	98 %
S/C ratio	2.5
Electrochemical compression	50 bar
Cell characteristics	
	$R_{\text{cell}} = 0.5 \text{ ohm cm}^2$
	Current density = 0.46 A cm ⁻²
	Nernst voltage = 0.126 V
	Cell voltage = 0.356 V
	Total power = 0.164 W cm ⁻²
	Area = 2.70 m ²
Heat losses in PMR	10%
Inlet temperature	450 °C
Outlet temperature	800 °C
Operation pressure	10 bar

Supplementary Figure 8 | Heat model for the PMR system. a, Heat required for the PMR system (reaction and heat for steam generation and heating up gasses) and heat given by the membrane with varying current density at 800 °C, 10 bar and 98 % HR, S/C = 2.5, and electrochemical compression up to 50 bar, showing an optimal heat balance at ~0.5 A cm⁻². **b**, Model assumptions and parameters of the electrochemical cell operating at 0.5 A cm⁻² for the distributed hydrogen production facility (10 kg H₂ day⁻¹).



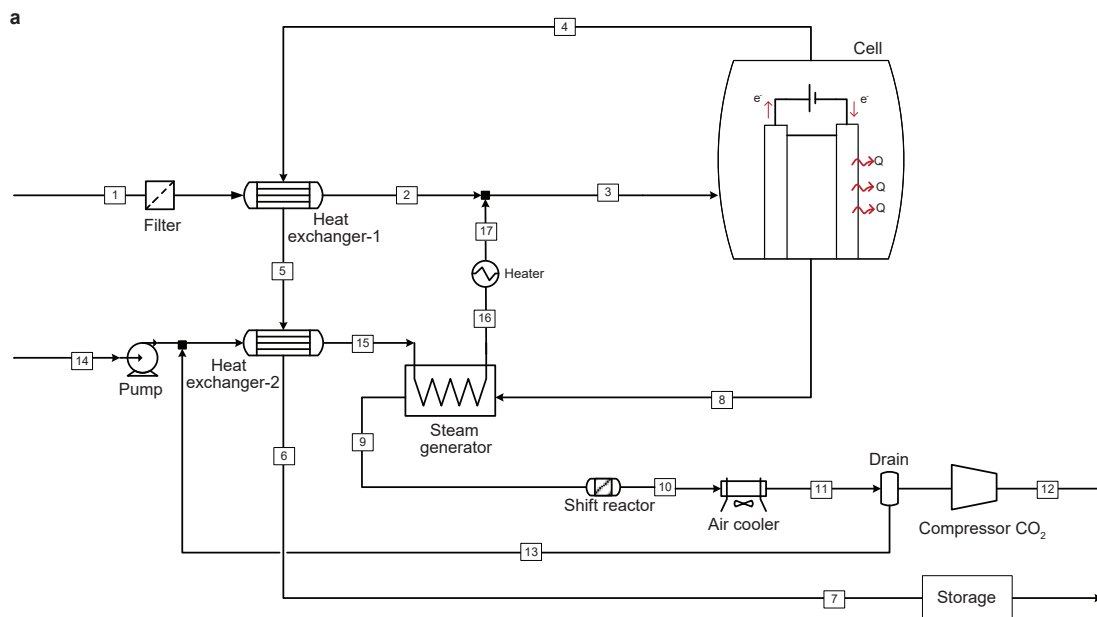
b

	1	2	3	4	5	6	7	8	9	10	11	12	13	14	15	16
Temperature (°C)	20.0	541.1	450.0	800.0	571.1	200.4	20.0	800.0	120.0	80.0	80.0	80.0	20.0	180.4	180.4	388.0
Pressure (bar)	10.0	10.0	10.0	50.0	50.0	50.0	200.0	10.0	10.0	10.0	10.0	10.0	1.0	10.0	10.0	10.0
Mass flow (kg day ⁻¹)	21.6	21.6	78.5	10.1	10.1	10.1	10.1	68.4	68.4	68.4	57.6	10.8	46.1	56.9	56.9	56.9
Composition (%)																
CH ₄	97.0	97.0	28.3	0.0	0.0	0.0	0.0	0.0	0.0	0.0	0.0	0.0	0.0	0.0	0.0	0.0
H ₂ O	0.0	0.0	70.8	0.0	0.0	0.0	0.0	31.8	31.8	31.8	4.6	100.0	100.0	100.0	100.0	100.0
CO	0.0	0.0	0.0	0.0	0.0	0.0	0.0	7.5	7.5	7.5	10.5	0.0	0.0	0.0	0.0	0.0
CO ₂	0.2	0.2	0.1	0.0	0.0	0.0	0.0	55.5	55.5	55.5	77.6	0.0	0.0	0.0	0.0	0.0
H ₂	0.0	0.0	0.0	100.0	100.0	100.0	100.0	4.7	4.7	4.7	6.6	0.0	0.0	0.0	0.0	0.0
O ₂	0.0	0.0	0.0	0.0	0.0	0.0	0.0	0.0	0.0	0.0	0.0	0.0	0.0	0.0	0.0	0.0
N ₂	0.9	0.9	0.3	0.0	0.0	0.0	0.0	0.5	0.5	0.5	0.7	0.0	0.0	0.0	0.0	0.0
C ₂ H ₆	1.4	1.4	0.4	0.0	0.0	0.0	0.0	0.0	0.0	0.0	0.0	0.0	0.0	0.0	0.0	0.0
C ₃ H ₈	0.6	0.6	0.2	0.0	0.0	0.0	0.0	0.0	0.0	0.0	0.0	0.0	0.0	0.0	0.0	0.0

c

Assumptions and parameters for hydrogen production process	
Hydrogen production	10 kg day ⁻¹
Hydrogen recovery	98 %
Cell	Pre-reforming at T = 450 °C (Modelled as Gibbs reactor) Reforming at T = 800 °C Operation pressure = 10 bar S/C ratio = 2.5
Heat exchanger -1	Δp/p = 2% Minimum ΔT = + 30 ° C (gas-gas)
Heat exchanger -2	Δp/p = 2% Minimum ΔT = + 20 ° C (Liquid-gas)
Compressor	Isoentropic. Multi stage compressor Efficiency = 85 % Discharge pressure 200 bar
Pump	Efficiency = 90 % Discharge pressure 10 bar
Condenser	Operation temperature = 80 ° C Operation pressure = 10 bar
Steam generator	Δp/p = 2% Efficiency = 80 %
Electric heater	Outlet temperature = 388 ° C

Supplementary Figure 9 | Balance of plant model for distributed hydrogen production facility (10 kg H₂ day⁻¹). **a**, Process flow diagram. **b**, Conditions and compositions of flow streams obtained from ASPEN simulations. Stream numbers are given in **(a)**. **c**, Assumptions and parameters of the ASPEN simulation for the distributed production facility.



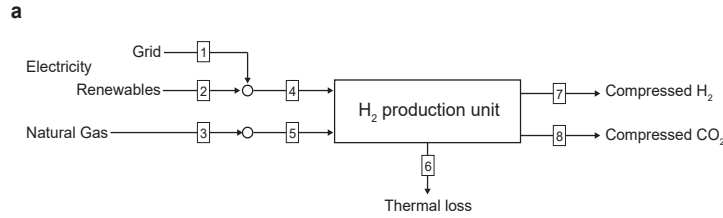
b

	1	2	3	4	5	6	7	8	9	10	11	12	13	14	15	16	17
Temperature (°C)	20.0	542.8	450.7	800.0	572.8	200.4	200.4	800.0	120.0	120.0	120.0	20.0	8.0	20.0	180.4	180.4	389.0
Pressure (bar)	26.0	26.0	26.0	26.0	26.0	26.0	26.0	26.0	26.0	26.0	26.0	153.0	26.0	1.0	26.0	26.0	26.0
Mass flow (tonne day ⁻¹)	1298.8	1298.8	4723.9	615.5	615.5	615.5	615.5	4103.5	4103.5	4103.5	4103.5	3469.5	634.0	3425.0	3425.0	3425.0	3425.0
Composition (%)																	
CH ₄	97.0	97.0	28.3	0.0	0.0	0.0	0.0	0.0	0.0	1.9	1.9	2.7	0.0	0.0	0.0	0.0	0.0
H ₂ O	0.0	0.0	70.8	0.0	0.0	0.0	0.0	30.4	30.4	30.4	30.4	0.05	100.0	100.0	100.0	100.0	100.0
CO	0.0	0.0	0.0	0.0	0.0	0.0	0.0	4.8	4.8	0.0	0.0	0.0	0.0	0.0	0.0	0.0	0.0
CO ₂	0.2	0.2	0.1	0.0	0.0	0.0	0.0	61.7	61.7	67.1	67.1	96.4	0.0	0.0	0.0	0.0	0.0
H ₂	0.0	0.0	0.0	100.0	100.0	100.0	100.0	2.6	2.6	0.0	0.0	0.0	0.0	0.0	0.0	0.0	0.0
O ₂	0.0	0.0	0.0	0.0	0.0	0.0	0.0	0.0	0.0	0.0	0.0	0.0	0.0	0.0	0.0	0.0	0.6
N ₂	0.9	0.9	0.3	0.0	0.0	0.0	0.0	0.6	0.6	0.6	0.6	0.8	0.0	0.0	0.0	0.0	0.0
C ₂ H ₆	1.4	1.4	0.4	0.0	0.0	0.0	0.0	0.0	0.0	0.0	0.0	0.0	0.0	0.0	0.0	0.0	0.0
C ₃ H ₈	0.6	0.6	0.2	0.0	0.0	0.0	0.0	0.0	0.0	0.0	0.0	0.0	0.0	0.0	0.0	0.0	0.0

c

Assumptions and parameters for hydrogen production process	
Hydrogen production	615.5 tonne day ⁻¹
Hydrogen recovery	99 %
Cell	Pre-reforming at T = 450 °C (Modelled as Gibbs reactor) Reforming at T = 800 °C Operation pressure = 26 bar S/C ratio = 2.5
Heat exchanger -1	Δp/p = 2% Minimum ΔT = + 30 °C (gas-gas)
Heat exchanger -2	Δp/p = 2% Minimum ΔT = + 20 °C (Liquid-gas)
Compressor CO ₂	Isoentropic Efficiency = 85 % Discharge pressure 153 bar
Pump	Efficiency = 90 % Discharge pressure 26 bar
Condenser	Operation temperature = 8 °C Operation pressure = 26 bar
Steam generator	Δp/p = 2% Efficiency = 80 %
Heater	Outlet temperature = 389 °C
Shift reactor	Modelled as Gibbs reactor Operation temperature = 120 °C

Supplementary Figure 10 | Balance of plant model for centralised hydrogen production facility (616 tonne H₂ day⁻¹) a, Process flow diagram. b, Conditions and compositions of flow streams obtained from ASPEN simulations. Stream numbers are given in (a). c, Assumptions and parameters of the ASPEN simulation for the centralised production facility.

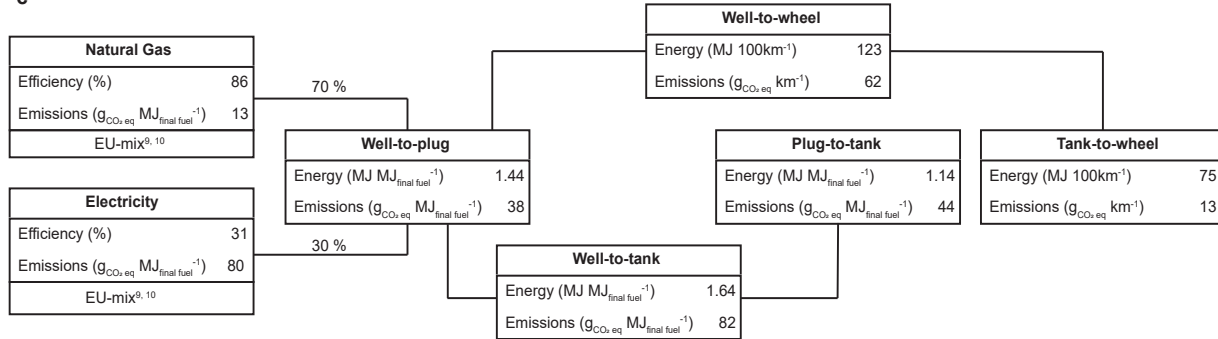


b

	1	2	3	4	5	6	7	8	
	CO ₂ emission intensity (g _{CO₂} MJ ⁻¹)			Inlet percentage ^s (MJ MJ ⁻¹)		Loss ^s (%)	Pressure (bar)	Capture efficiency (%)	Capture pressure (bar)
WEL Centralised	76.6	0	na	100.0	0.0	na/32	26	na	na
Distributed	-	-	na	100.0	0.0	na/38	200	na	na
SMR-1 Centralised	76.6	0	69.0	2.0/0.6	98.0/99.4	27.2/24.2	26	66.2	153
Distributed	-	-	69.0	na/13.0	na/87.0	na/36	200	na	na
SMR-2 Centralised	76.6	0	69.0	2.4/0.6	97.6/99.4	30.2/24.2	26	90.0	153
PMR Centralised	76.6	0	69.0	27.7/26.1	72.3/73.9	6.9/4.9	26	100	153
Distributed	-	-	69.0	30.4	69.6	na/32	200	na	na

^sWith/without capture

c



d

	Well-to-tank		Tank-to-wheel	
	Energy (MJ 100km ⁻¹)	GHG emissions (g _{CO₂} eq km ⁻¹)	Energy (MJ 100km ⁻¹)	GHG emissions (g _{CO₂} eq km ⁻¹)
ICE*	38	29	204	151
BEV	116	78	52	0
WEL	213	112	75	0

*ICE: Gasoline DISI (Direct Injection Spark Ignition technology). BEV: EU-mix

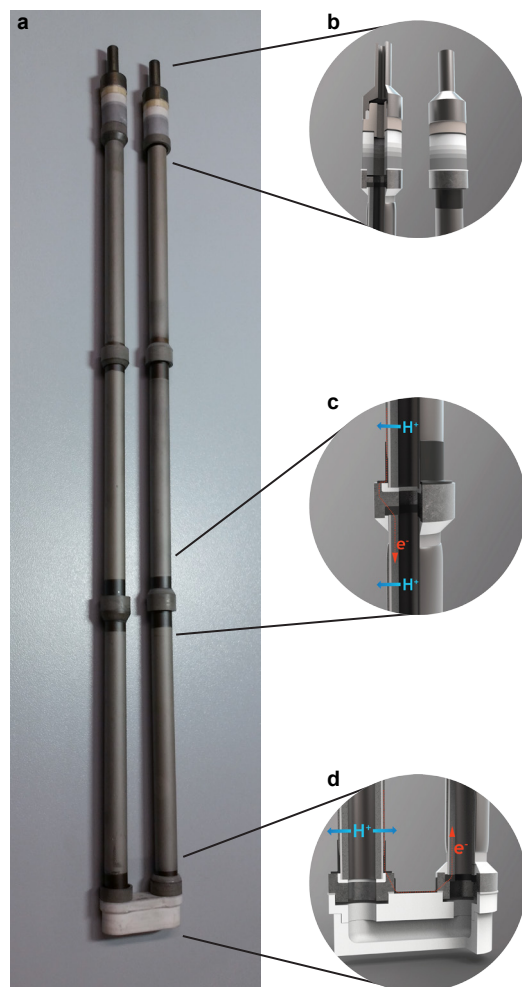
e

	GHG emissions (kg _{CO₂} eq kg _{H₂} ⁻¹) from centralised plants		
	Grid	RE	RE+CC
WEL	16.0	0	na
SMR	12.9	12.8	6.1
PMR	10.6	7.2	1.4

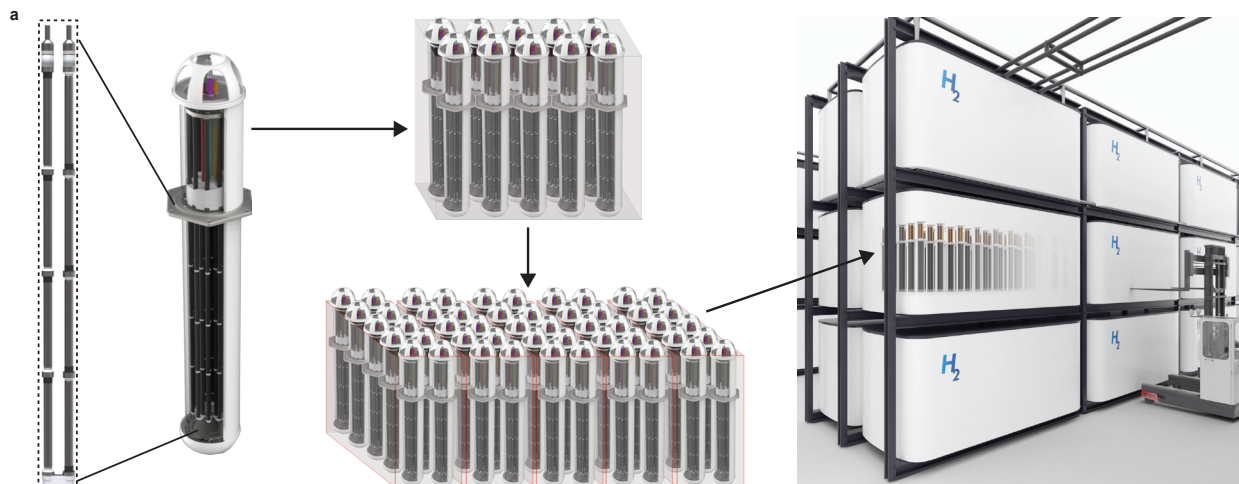
f

Region & Market	Time Period	Data Source	Electric to Gas Price Ratio
Texas (U.S), Industrial customer	Sept 2016	Electric: 0.053 USD/kWh Natural Gas: 3.16 USD/thousand ft ³ Source: U.S. Energy Information Administration	5.3
Norway (Europe), Industrial customer	Q3 2016	Electric: 0.27 NOK/kWh Natural Gas: 1.5 NOK/Standard m ³ Source: Statics Norway, National Budget	2.0
EU-28 (Europe), Industrial customer	1 ST half 2016	Electric: 0.117 EUR/kWh Natural Gas: 0.032 EUR/kWh Source: Eurostat	3.7
EU-28 (Europe), Commercial customer	1 ST half 2016	Electric: 0.206 EUR/kWh Natural Gas: 0.062 EUR/kWh Source: Eurostat	3.3

Supplementary Figure 11 | Techno-economic evaluation of PMR technology. **a**, Schematic representation of techno-economic evaluation of hydrogen production technologies. **b**, Summary of inputs and assumptions for the evaluation (see Methods for details). **c**, Schematic representation of well-to-wheel calculation. **d**, Breakdown of well-to-wheel analysis in terms of efficiencies and greenhouse gas (GHG) emissions for battery electric vehicle (BEV) and internal combustion engine (ICE). See Methods for details. **e**, GHG emissions of the expended energy for the production of hydrogen in centralised plants using grid electricity, renewable electricity (RE) or RE nad with carbon capture (RE+CC) for the SMR and PMR plants. **f**, Electricity to natural gas price ratio in different regions and markets. Prices normalised to \$ GJ⁻¹ before calculating the ratio.



Supplementary Figure 12 | Segmented six-tube PMR reactor. **a**, Optical image of six membrane tubes (10 cm electrode length each) segmentally connected with sealed interconnects to a gradient connector and a single chamber gas manifold (“U-bend”). **b**, Schematic of a CTE gradient connector allowing for the connection of membrane tubes to the outside metallic pressure vessel, expanding CTEs of 8.6 - 11 ppm K^{-1} . **c**, Schematic of interconnect and glass seals, showing proton paths and also the electron path from the outer electrode of one tube to the inner electrode of the next segmented tube. **d**, Schematic of the single chamber gas manifold, connecting two 3-tube segments with both gas and electrical flow.



b

SEU characteristics			
Hydrogen production rate (lean mode)			2.3 kg day ⁻¹
Pressure vessel	Design pressure	31 barg	
	Material	Alloy 800HT	
	Outer diameter	116 mm	
	Wall thickness	8 mm	
	Height	1150 mm	
Ceramic cell	Outer diameter	10 mm	
	Active electrode length	186 mm	
	Current density	0.54 A cm ⁻²	
	Nernst voltage	0.054 V	
	Cell voltage	0.323 V	
	Power density	0.174 W cm ⁻²	

c

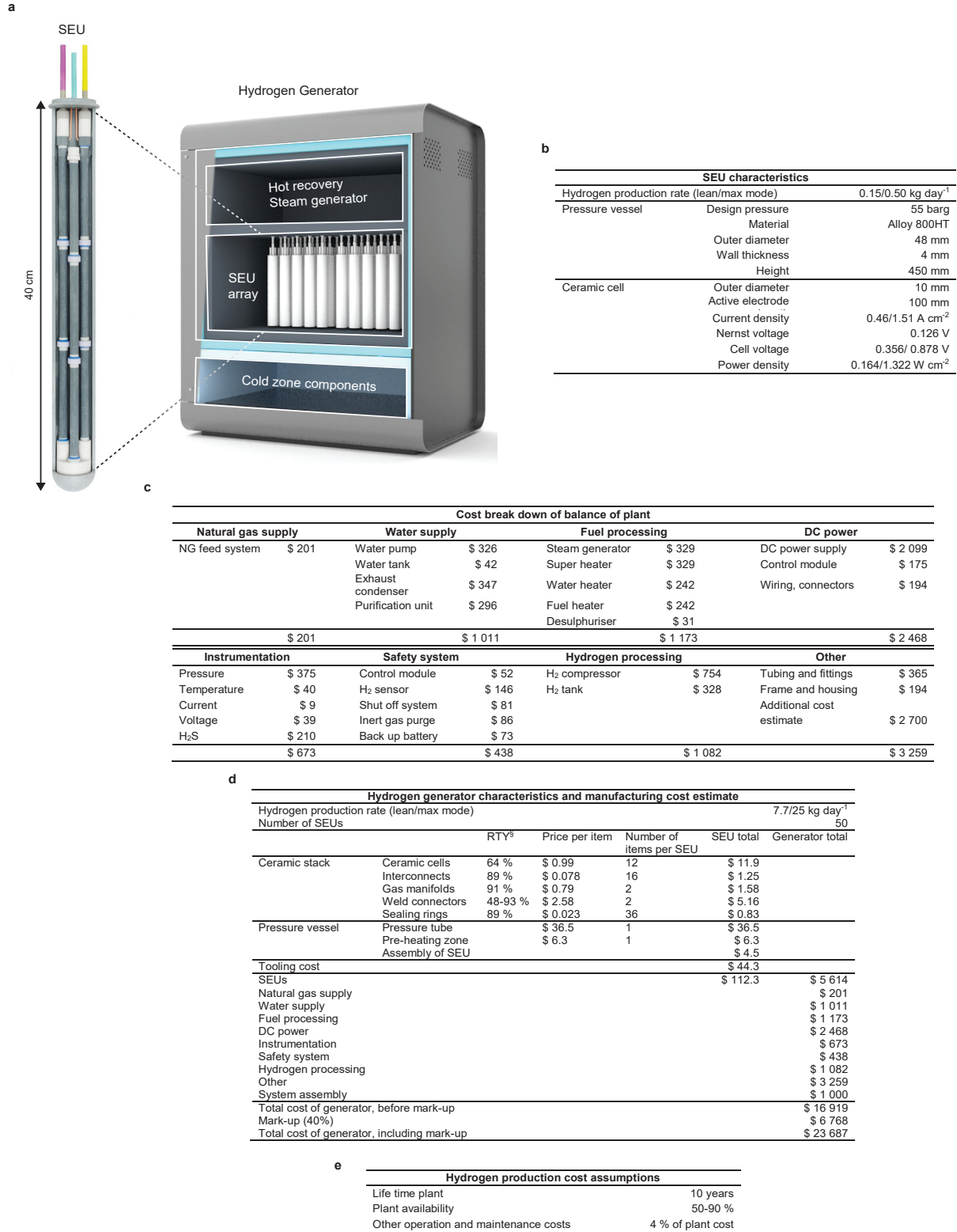
Main raw materials, usage (including scrap), and price to produce one SEU			
Material	Usage (kg)	Price (\$ kg ⁻¹)	SEU total (\$)
BaSO ₄	2.96	2	5.93
CeO ₂	0.44	4	1.75
ZrO ₂	1.10	8	8.77
Y ₂ O ₃	0.14	15	2.16
NiO	2.76	27	74.6
ZTA	0.38	15	5.76
Alloy 800 HT	25.5	15	382

d

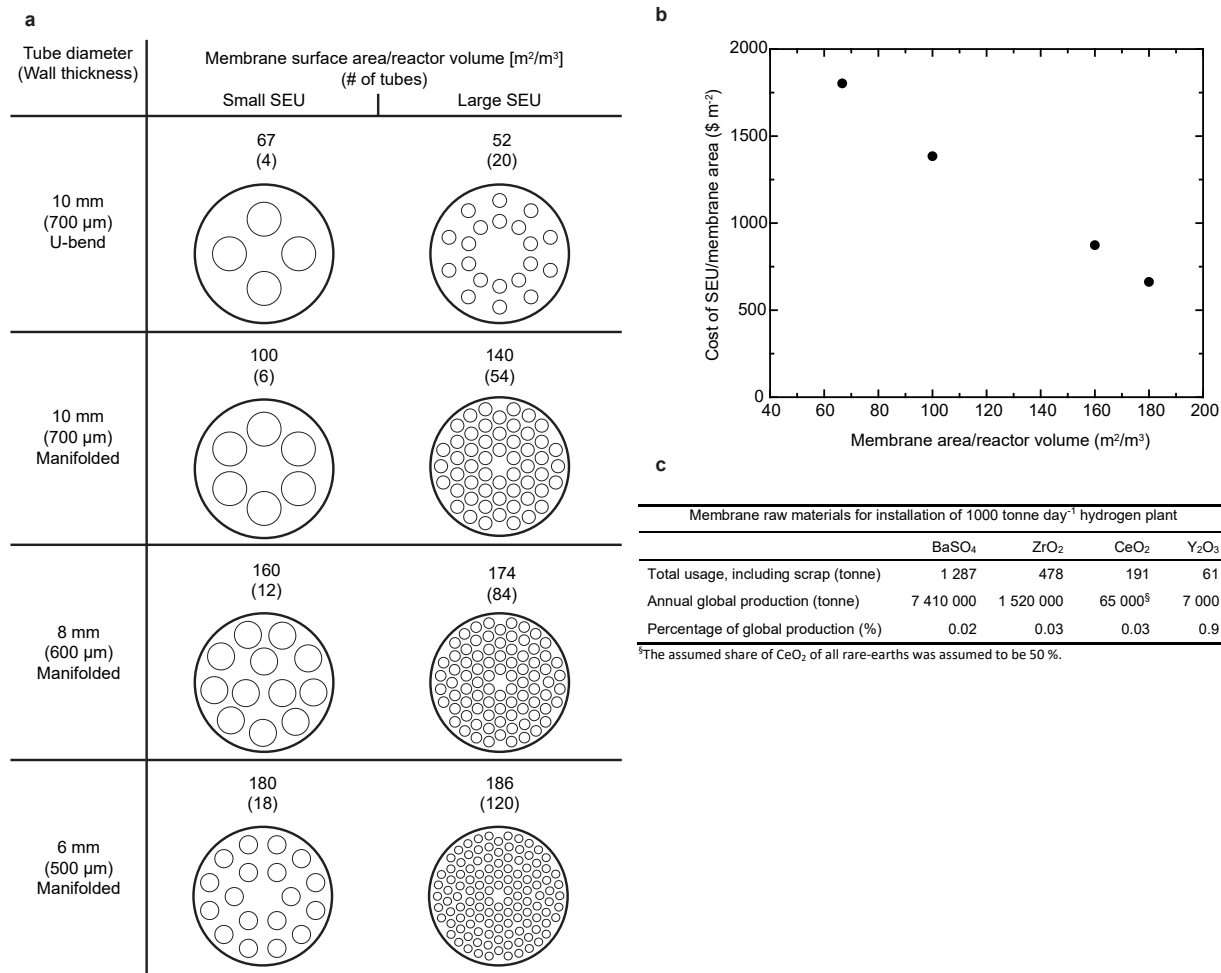
Module characteristics and manufacturing cost estimate						
Hydrogen production rate (lean mode)			230 kg day ⁻¹			
Number of SEUs			100			
		RTY [§]	Price per item	Number of items per SEU	SEU total	Module total
Ceramic stack	Ceramic cells	64 %	\$ 1.44	80	\$ 115	
	Interconnects	89 %	\$ 0.072	100	\$ 7.2	
	Gas manifolds	91 %	\$ 0.68	10	\$ 6.8	
	Weld connectors	48-93 %	\$ 2.58	20	\$ 51.6	
	Sealing rings	89 %	\$ 0.001	240	\$ 0.2	
Pressure vessel	Pressure tube		\$ 390	1	\$ 390	
	Pre-heating zone		\$ 51.6	1	\$ 51.6	
	Assembly of SEU				\$ 22.4	
Tooling cost					\$ 290	
SEUs					\$ 934	\$ 93.4 k
Instrumentation						\$ 1.5 k
Tubing and fittings						\$ 2.0 k
Housing						\$ 1.5 k
Safety system						\$ 1.0 k
System assembly						\$ 3.0 k
Total cost of module, before mark-up						\$ 102.4 k
Mark-up (40%)						\$ 41.0 k
Total cost of module, including mark-up						\$ 143.4 k

[§] Rolled throughput yield

Supplementary Figure 13 | Conceptual design for manufacturing cost estimate of membrane module for centralised hydrogen plant. **a**, Conceptual design of module. The module comprises 100 single engineering units (SEUs), and a SEU consist of 80 ceramic cells. **b**, Main characteristics of SEU. **c**, Main raw materials used to produce one SEU, the usage and the assumed price used for the cost estimates. Material usage include scrap. **d**, Module characteristics and manufacturing cost estimate.



Supplementary Figure 14 | Conceptual design for manufacturing cost estimate of hydrogen generator for distributed production of hydrogen. a, Conceptual design of hydrogen generator. The generator comprises 50 single engineering units (SEUs). Each SEU consist of 12 ceramic cells. **b,** Main characteristics of SEU. **c,** Cost breakdown of balance of plant associated to the hydrogen generator. **d,** Hydrogen generator characteristics and manufacturing cost estimate. **e,** Hydrogen production cost assumptions.



Supplementary Figure 15 | Scalability of PMR design. **a**, Table of tube layouts for small and large single engineering units (SEU) for a 10 mm tube diameter single chamber “U-bend” design (as shown in Supplementary Figure 12) and for manifolded 10, 8, and 6 mm diameter tube reactors. **b**, Cost of SEU per membrane area versus ratio of membrane area to reactor volume. Price decreases when packing density increases. **c**, Usage of raw materials for installation of plant with hydrogen production capacity of 1000 tonne day⁻¹. Usage is compared with annual global production volume (2015, except Y₂O₃ were data if from 2016). Data source: Mineral Commodity Summaries 2017, US Geological Survey.

Supplementary Table 1 | Table for equations used in the thermo-fluid dynamic simulations. u : velocity; p : pressure; I : identity matrix; ϵ_p : porosity of the cell support; κ : permeability in the cell support, βF : isothermal compressibility coefficient; Q_{br} : the source term; j_i : weight flux for the i compound; w_i : weight fraction, R_i : source term for the compound i ; N_i : weight flow for the i compound; $D_i T$: thermal diffusion coefficient for the compound i (neglected for this study); i_i : ionic current density; Q_i : ionic current density source term; σ_i : ionic conductivity; ϕ_i : ionic potential; i_s : electric current density; Q_s : electric current density source term; σ_s : electric conductivity; ϕ_s : electric potential; C_p is the heat capacity; k is the thermal conductivity; Q is the heat source and θ_p is the volumetric fraction of the internal electrode, f_i : fugacity of the compound i .

Model	Domains	Description	Equation	Id	
	Gas chambers	Governing	$\rho(u\bar{v})u = \nabla \left[-pI + \mu (\nabla u + (\nabla u)^T) - \frac{2}{3} u (\nabla \cdot u) \right]$	M1	
		Boundary conditions	$\nabla(\rho u) = 0$	M2	
	Porous cermet	Governing	$\frac{\rho}{\epsilon_p} \left((u\bar{v}) \frac{u}{\epsilon_p} \right) = \nabla \left(-pI + \frac{\mu}{\epsilon_p} (\nabla u + (\nabla u)^T) - \frac{2\mu}{3\epsilon_p} u (\nabla \cdot u) \right) - \left(\mu \kappa^{-1} + \beta F u + \frac{Q_{br}}{\epsilon_p} \right) u + F_{vol}$	M3	
		Boundary conditions	$\nabla(\rho u) = Q_{br}$	M4	
Fluid flow		Density	$\rho_i = \frac{p_i}{RT} \cdot M_{N_i}$ (i : chamber)	M5	
		Properties	Viscosity (internal gas)	$\mu_{gm} = \sum_i \frac{1}{1 + \frac{1}{x_i} \sum_{j \neq i} x_j \phi_{ij}}$	M6
			Wilke dimensionless number	$\phi_{ij} = \frac{\left(1 + \left(\frac{\mu_i}{\mu_j} \right)^{1/2} \left(\frac{M_j}{M_i} \right)^{1/4} \right)^2}{\frac{4}{\sqrt{2}} \left(1 + \frac{M_i}{M_j} \right)^{1/2}}$	M7
Species transport	Internal gas	Governing	$\nabla_j + \rho(u\bar{v})w_j = R_i$ $N_i = j_i + \rho \cdot u \cdot w_i$	M8 M9	
		Governing	$j_i = - \left(\rho D_i^m \nabla w_i + \rho w_i D_i^m \frac{\nabla M_n}{M_n} + D_i^m \frac{\nabla T}{T} \right)$	M10	
		Average diffusivity for compound	$D_i^m = \frac{1 - w_i}{\sum_{k \neq i} \frac{x_k}{D_{i,k}}}$	M11	
		Average molecular weight	$M_n = \left(\sum_i \frac{w_i}{M_i} \right)^{-1}$	M12	
		Permeability for a packed-bed	$\kappa = \frac{d_p^2 \epsilon_p^3}{150(1 - \epsilon_p)^2}$	M13	
		Maxwell-Stefan diffusivity	$D_{i,j} = \kappa \frac{T^{1.75}}{p \left(\sqrt{1/3} - \sqrt{1/3} \right) \left(\frac{1}{M_i} + \frac{1}{M_j} \right)^{1/2}}$	M14	
Charge	Electrode and electrolyte	Governing	$\nabla i_l = Q_l$ $i_i = -\sigma_i \nabla \phi_i$ $\nabla i_s = Q_s$ $i_s = -\sigma_s \nabla \phi_s$	M15 M16 M17 M18	
		Overpotential	$\eta = \phi_s - \phi_l - E_{eq}$	M19	
		Nernst equation	$E_{rev,ri} = E_{rev}^0 + \frac{RT}{zF} \ln \left(\prod_i f_i^{y_i} \right)$	M20	
		Total area specific resistance	$R_{a,th} = 0.5 \Omega \text{ cm}^2 \exp \left(\frac{50.4 \text{ kJ mol}^{-1}}{R_g} \left(\frac{1}{T} - \frac{1}{1073.15 \text{ K}} \right) \right)$	M21	
		Governing	$\rho C_p u \cdot \nabla T = \nabla(k \nabla T) + Q$	M22	
		Governing	$\rho C_p u \cdot \nabla T = \nabla(k_{eq} \nabla T) + Q$	M23	
		Thermal conductivity correction	$k_{eq} = \theta_p \kappa_p + (1 - \theta_p) \kappa$	M24	
Energy	Internal gas	Properties	Heat capacity	$C_{p,gm} = \sum_i C_{p,i} x_i$	M25
			Thermal conductivity	$k_{gm} = \sum_i \frac{k_i}{1 + \frac{1}{x_i} \sum_{j \neq i} x_j \phi_{ij}}$	M26
		Internal electrode	Reaction heats	$\text{Heat}_{ri}(T) = -\Delta H_{ri}(T) \cdot r_i$	M27
Electrolyte	Joule effect	$\text{Heat}_{joule} = \frac{ASR(T)}{\text{Area}} \cdot I_{ca}^2$	M28		
Internal electrode	Compression	$\text{Heat}_{compression} = RT \ln \left(\frac{P_{H_2, external}}{x_{H_2} \cdot P_{H_2, internal}} \right)$	M29		
Reaction	Internal electrode	Steam reforming rate	$r_{SMR} = k_{SMR}(T) f_{CH_4} f_{H_2O} \left(1 - \frac{f_{CO}^3 f_{H_2}}{f_{CH_4} f_{H_2O} K_{EQ,SMR}(T)} \right)$	M30	
		Water shift reaction rate	$r_{WGS} = k_{WGS} f_{CO} f_{H_2O} \left(1 - \frac{f_{CO_2} f_{H_2}}{f_{CO} f_{H_2O} K_{EQ,WGS}(T)} \right)$	M31	
		Equilibrium	$K_{EQ,ri} = p^{\Delta n_i} \exp \left(-\frac{\Delta G_{ri}}{R_g T} \right)$	M32	
		SR kinetic constant	$k_{SMR}(T) = k^0_{SMR} \exp \left(-\frac{E_{act,SMR}}{R_g T} \right)$	M33	

Supplementary Table 2 | Cost break down and assumptions for centralised hydrogen production plants. a, Cost breakdown of protonic membrane reformer plant. **b,** Cost breakdown of steam methane reformer plant. **c,** Cost breakdown of water electrolyser plant. **d,** Assumptions for hydrogen production cost calculations.

a

SMR plant cost summary	
Component	\$ 1000
Externally heated SMR reactor	64 608
Sulphur removal unit	271
Air compressor	962
Water-gas shift reactor	14 429
Amine scrubber for CO ₂ removal	107 215
CO ₂ compressor and drier	13 626
Pressure swing adsorber	42 498
Water boiler	8 161
Balance of plant (15 % of installed equipment)	37 766
Engineering and construction management (10 %)	28 954
Process contingency (20 % for CO ₂ removal)	21 443
Project contingency (20 %)	57 908
Plant cost - baseline	397 842

b

PMR plant cost summary	
Component	\$ 1000
Membrane modules	385 646
Sulfur removal unit	271
Heat exchangers	4 810
CO ₂ compressor and drier	18 424
Water boiler	8 161
DC power supply (240 MW)	19 200
Balance of plant (15 % of installed equipment)	7 630
Engineering and construction management (10 %)	5 850
Project contingency (20 %)	88 828
Plant cost - baseline	538 819

c

WEL plant cost summary	
System efficiency: 68 %	
Energy input: 57.9 kWh/kg	
Required power: 1488 MW	
Electrolyser cost	651 \$ kW ⁻¹
Compression cost	107 \$ kW ⁻¹
Grid connection	32 \$ kW ⁻¹
Total	790 \$ kW ⁻¹
Plant cost - baseline	\$ 1 175 675 000

d

Hydrogen production cost assumptions		
Life time plant		20 years
Plant availability		90 %
Fixed operation and maintenance		2 % of plant cost
Ranges for plant cost estimates	Minimum	Maximum
SMR (project contingency)	0	40 %
WEL (electrolyser cost)	395 \$ kW ⁻¹	908 \$ kW ⁻¹
PMR (Membrane module cost)	\$ 246 205 000	\$ 385 646 000
PMR (project contingency)	20 %	40 %

Supplementary References

1. Buddenberg, J.W. & Wilke, C.R. Calculation of Gas Mixture Viscosities. *Ind. Eng. Chem. Res.* **41**, 1345-1347, doi:10.1021/ie50475a011 (1949).
2. Nield, D.A. & Bejan, A. *Convection in Porous Media*. 4 edn, (Springer-Verlag, 2013).
3. Zeppieri, M., Villa, P.L., Verdone, N., Scarsella, M. & De Filippis, P. Kinetic of methane steam reforming reaction over nickel- and rhodium-based catalysts. *Appl. Catal. A* **387**, 147-154, doi:<http://dx.doi.org/10.1016/j.apcata.2010.08.017> (2010).
4. Wang, B., Zhu, J. & Lin, Z. A theoretical framework for multiphysics modeling of methane fueled solid oxide fuel cell and analysis of low steam methane reforming kinetics. *Appl. Energy* **176**, 1-11, doi:<http://dx.doi.org/10.1016/j.apenergy.2016.05.049> (2016).
5. Aguiar, P., Adjiman, C.S. & Brandon, N.P. Anode-supported intermediate temperature direct internal reforming solid oxide fuel cell. I: model-based steady-state performance. *J. Power Sources* **138**, 120-136, doi:<http://dx.doi.org/10.1016/j.jpowsour.2004.06.040> (2004).
6. Shirasaki, Y. *et al.* Development of membrane reformer system for highly efficient hydrogen production from natural gas. *Int. J. Hydrog. Energy* **34**, 4482-4487, doi:<http://dx.doi.org/10.1016/j.ijhydene.2008.08.056> (2009).
7. Kume, T. *et al.* Development of compact and efficient hydrogen production module with membrane on catalyst. *J. Nat. Gas Sci. Eng.* **3**, 591-600, doi:<http://dx.doi.org/10.1016/j.jngse.2011.07.010> (2011).
8. Boeltken, T., Wunsch, A., Gietzelt, T., Pfeifer, P. & Dittmeyer, R. Ultra-compact microstructured methane steam reformer with integrated Palladium membrane for on-site production of pure hydrogen: Experimental demonstration. *Int. J. Hydrog. Energy* **39**, 18058-18068, doi:<http://dx.doi.org/10.1016/j.ijhydene.2014.06.091> (2014).
9. Edwards, R. *et al.* *Well-To-Wheels analysis of future automotive fuels and powertrains in the european context, Well-to-Wheels Report Version 4.a, JEC Well-to-Wheels Analysis*. (Joint Research Centre, 2014). <http://iet.jrc.ec.europa.eu/about-jec/>.
10. Huss, A., Maas, H. & Hass, H. *Well-to-Wheels analysis of future automotive fuels and powertrains in teh european context, Tank-to-Wheels Report Version 4.0, JEC Technical Reports*. (Joint Research Centre, 2013). <http://iet.jrc.ec.europa.eu/about-jec/>.